Publications of the Astronomical Society of the Pacific, 128:055004 (21pp), 2016 May doi:10.1088/1538-3873/128/963/055004
© 2016. The Astronomical Society of the Pacific. All rights reserved. Printed in the U.S.A.

Vision: A Six-telescope Fiber-fed Visible Light Beam Combiner for the Navy Precision Optical Interferometer

Eugenio V. Garcia[1,2], Matthew W. Muterspaugh[3,4], Gerard van Belle[1], John D. Monnier[5], Keivan G. Stassun[2], Askari Ghasempour[6], James H. Clark[7], R. T. Zavala[8], James A. Benson[8], Donald J. Hutter[8], Henrique R. Schmitt[7], Ellyn K. Baines[7], Anders M. Jorgensen[9], Susan G. Strosahl[1], Jason Sanborn[1], Stephen J. Zawicki[1], Michael F. Sakosky[1], and Samuel Swihart[10]
[1] Lowell Observatory, Flagstaff, AZ 86001, USA; eugenio.v.garcia@gmail.com
[2] Department of Physics & Astronomy, Vanderbilt University, 6301 Stevenson Science Center, Nashville, TN 37212, USA
[3] Department of Mathematical Sciences, College of Life and Physical Sciences, Tennessee State University, Boswell Science Hall, Nashville, TN 37209, USA
[4] Center of Excellence in Information Systems Engineering and Management, Tennessee State University, 3500 John A. Merritt Boulevard, Box No. 9501, Nashville, TN 37209-1561, USA
[5] University of Michigan (Astronomy), 500 Church Street, Ann Arbor, MI 48109, USA
[6] Optical Spectroscopsy Division, HORIBA Scientific, 3880 Park Avenue, Edision, NJ 08820, USA
[7] Remote Sensing Division, Naval Research Laboratory, 4555 Overlook Avenue SW, Washington, DC 20375, USA
[8] U.S. Naval Observatory, Flagstaff Station, 10391 W. Naval Observatory Road, Flagstaff, AZ 86005, USA
[9] Electrical Engineering Department, New Mexico Institute of Mining and Technology, Socorro, NM, USA
[10] Michigan State University, 3265 Biomedical and Physical Sciences Building, Okemos, MI 48864, USA
Received 2015 October 30; accepted 2015 December 30; published 2016 April 5

Abstract

Visible-light long baseline interferometry holds the promise of advancing a number of important applications in fundamental astronomy, including the direct measurement of the angular diameters and oblateness of stars, and the direct measurement of the orbits of binary and multiple star systems. To advance, the field of visible-light interferometry requires development of instruments capable of combining light from 15 baselines (6 telescopes) simultaneously. The Visible Imaging System for Interferometric Observations at NPOI (VISION) is a new visible light beam combiner for the Navy Precision Optical Interferometer (NPOI) that uses single-mode fibers to coherently combine light from up to six telescopes simultaneously with an image-plane combination scheme. It features a photometric camera for calibrations and spatial filtering from single-mode fibers with two Andor Ixon electron multiplying CCDs. This paper presents the VISION system, results of laboratory tests, and results of commissioning on-sky observations. A new set of corrections have been determined for the power spectrum and bispectrum by taking into account non-Gaussian statistics and read noise present in electron-multipying CCDs to enable measurement of visibilities and closure phases in the VISION post-processing pipeline. The post-processing pipeline has been verified via new on-sky observations of the O-type supergiant binary ζ Orionis A, obtaining a flux ratio of 2.18 ± 0.13 with a position angle of $223\overset{\circ}{.}9 \pm 1\overset{\circ}{.}0$ and separation 40.6 ± 1.8 mas over 570–750 nm, in good agreement with expectations from the previously published orbit.

Key words: instrumentation: high angular resolution – instrumentation: interferometers – methods: data analysis – methods: observational – techniques: high angular resolution – techniques: interferometric

1. Introduction

A beam combiner coherently combines the starlight from the multiple telescopes of the interferometer to form interference patterns (fringes). These fringes are the Fourier components of the image of the object being observed and thus allow for the measurement of the angular diameters of stars, the orbits of binary and multi-star systems with milliarcsecond separations, and the direct observation of stellar surface features. The advantage of optical interferometry is high angular resolution typically in the milliarcsecond or sub-milliarcsecond range.

Over the past two decades, visible-light beam combiners have been commissioned for three interferometers: the Navy Precision Optical Interferometer (NPOI, Armstrong et al. 1998b), the Center for High Angular Resolution Astronomy (CHARA) Array (ten Brummelaar et al. 2005), and the Sydney University Stellar Interferometer (SUSI, Davis et al. 1999a, 1999b). Currently, visible-light beam combiners being commissioned or recently made operational are the Precision Astronomical Visible Observations (PAVO) for the CHARA Array and SUSI (Ireland et al. 2008; Maestro et al. 2012, 2013), the Micro-arcsecond University of Sydney Companion Astrometry instrument for SUSI (Kok et al. 2012), and the Visible spEctroGraph and polArimeter (VEGA, Mourard et al. 2008, 2009, 2011, 2012) for CHARA. In addition, at NPOI there is the "Classic" pupil-plane combiner (Mozurkewich 1994), which is having its fringe engine upgraded (Sun

et al. 2014; Landavazo et al. 2014), and is named the New Classic fringe engine. All of these beam combiners have provided insights into rapidly rotating stars (Ohishi et al. 2004; Peterson et al. 2006; Jamialahmadi et al. 2015), direct measurements of stellar radii (Armstrong et al. 2001, 2012; Wittkowski et al. 2006; North et al. 2007, 2009; Bazot et al. 2011; Baines et al. 2013, 2014; Challouf et al. 2014; Jorgensen et al. 2014), validation of transiting exoplanets (Huber et al. 2012a, 2012b), and binary and multiple star systems (Hummel et al. 1998, 2001, 2003; Patience et al. 2008; Schmitt et al. 2009; Tango et al. 2009; Zavala et al. 2010; Hummel et al. 2013; Wang et al. 2015).

However, with the exception of the upgraded "Classic" fringe engine for the NPOI, none of these are yet capable of simultaneous measurement of fringes on all available baselines. Dense coverage of the UV plane is critical for making the first direct stellar surface images at visible wavelengths, and this is best accomplished by simultaneously observing a star with as many baselines as possible. This is one of main advantages of the Visible Imaging System for Interferometric Observations at NPOI (VISION), which has recently been commissioned and is described in this paper.

VISION's design was derived from the six-telescope Michigan InfraRed Combiner (MIRC, Monnier et al. 2004, 2006, 2007). VISION is a six-telescope, all-in-one beam combiner using single-mode fibers and visible light electron-multiplying charge coupled devices (EMCCDs). Prior to VISION and MIRC, the Integrated Optics Near-infrared Interferometric Camera instrument for the Infrared Optical Telescope Array (IOTA) (Rousselet-Perraut et al. 1999, 2000; Berger et al. 2003; Traub et al. 2004) to filter and guide light also used single mode fibers to measure closure phases (Ragland et al. 2004).

VISION was built by Tennessee State University in collaboration with Lowell Observatory, the United States Naval Observatory, and the Naval Research Laboratory (Ghasempour et al. 2012). It monitors individual telescope throughputs and fiber coupling efficiencies in real time for visibility calibration. VISION operates from 580 to 850 nm, whereas MIRC operates in the near-infrared (IR) at 1490–1750 nm (*H*-band). It is capable of simultaneously measuring 15 visibilities, 20 triple amplitudes, and 20 closure phases, allowing for dense UV plane coverage and image reconstruction.

VISION's six-telescope simultaneous beam combination allows for multi-pixel images across the surface of a target star via image reconstruction. VISION is intended to deliver complementary visible-light observations to MIRC's near-IR observations of rapidly rotating stars, binary stars, and red super giants (Monnier et al. 2007, 2012; Zhao et al. 2008; Che et al. 2011; White et al. 2013; Baron et al. 2014; Kloppenborg et al. 2015; Roettenbacher et al. 2015a, 2015b). Early science targets for VISION include imaging the surfaces of rapidly rotating stars and red supergiants for testing of 2D and 3D stellar models. It will be used to test 2D models of rapidly rotating stars (Espinosa Lara & Rieutord 2011, 2013) and 3D radiative-hydrodynamic models of red supergiants (Freytag et al. 2002; Freytag & Höfner 2008; Chiavassa et al. 2009, 2010, 2011, 2012); to date, only a few rapidly rotating stars and several red supergiants have been observed via interferometry (see reviews by Domiciano de Souza et al. 2003; Peterson et al. 2006; Monnier et al. 2007, 2012; Zhao et al. 2008; Haubois et al. 2009; Che et al. 2011; Domiciano de Souza et al. 2012; van Belle 2012; Baron et al. 2014).

Furthermore, VISION has high spatial resolution imaging coupled with a large field of view from moderate spectral resolution. This allows VISION to study hierarchical triple star systems, where one of the two components of a relatively wide pair of stars is itself a much more narrowly separated binary. VISION can measure the relative astrometry between the different components of the triple or quadruple system. There are only a handful of fully characterized orbits of multi-star systems (Hummel et al. 2003; Muterspaugh et al. 2005, 2006a, 2006b, 2006c, 2008, 2010).

This paper presents the design of the VISION instrument, laboratory tests evaluating the system performance, and validation of the data-processing pipeline from new on-sky resolved measurements of the O-type supergiant binary ζ Orionis A. In Section 2, the VISION optical design and light path is detailed. In Section 3 the data acquisition sequence is described. In Section 4 the throughput, cameras, system visibility, and fringe crosstalk are evaluated. In Section 5 the adaptation of the MIRC data-processing pipeline for VISION is described and the theoretical bispectrum and power spectrum bias subtraction equations for an EMCCD in the photon counting regime are evaluated. The post-processing pipeline is validated in Section 6 using on-sky commissioning observations of ζ Orionis A and new resolved astrometric measurements of the flux ratio, separation, and position angle of this benchmark binary star system are reported. Finally, in Section 7 a summary and a brief description of planned future work are discussed.

2. The VISION Instrument

2.1. Optical Design

The VISION optical design is shown in Figure 1, and the beam combiner itself in Figure 2. Similar to MIRC, VISION uses single-mode optical fibers that spatially filter incoming starlight, enabling precise visibility and closure phase measurements (Shaklan et al. 1992). Unlike MIRC, the VISION fibers are polarization-maintaining. The six outputs of VISION's single mode fibers are arranged in a non-redundant pattern using a V-groove array. The polarization of the starlight parallel to the optical bench is reflected by a polarizing beam splitter, focused into multimode fibers, which are reconfigured

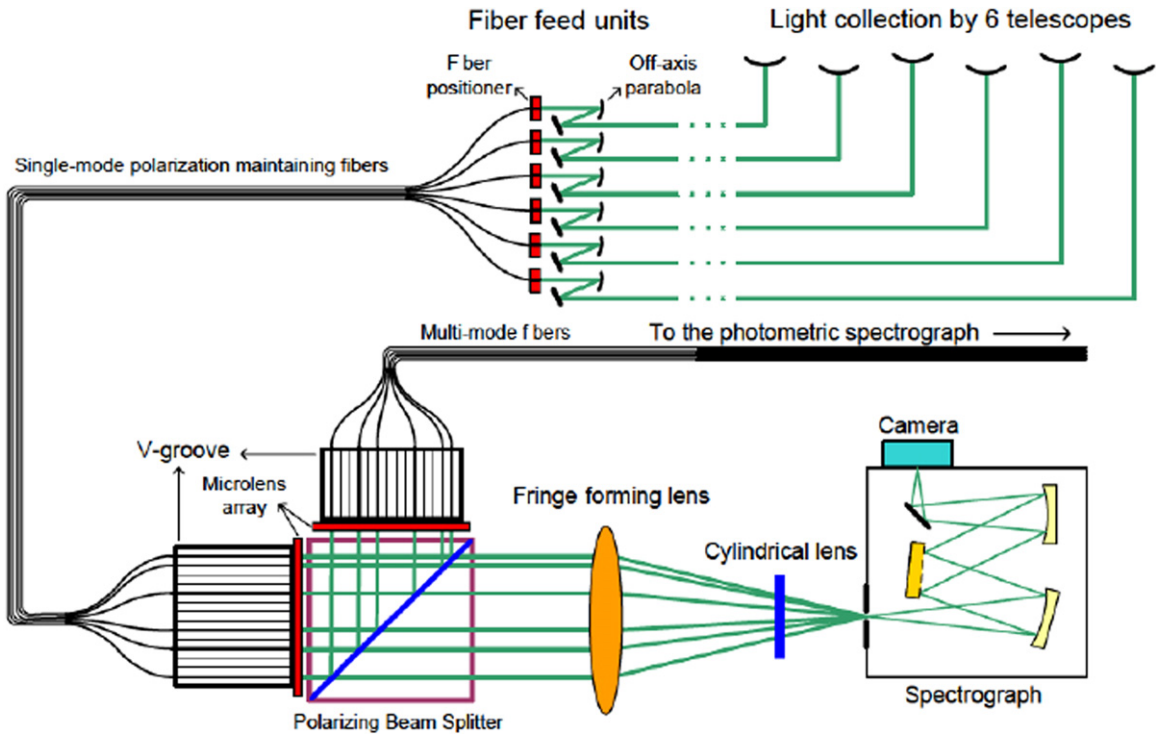

Figure 1. A diagram of light path for the VISION beam combiner. Light from up to six telescopes is coupled to single-mode polarization-maintaining fibers via off-axis parabolas and picomotor fiber positioners. Beam 6 has not yet been commissioned due to observatory maintenance. The single-mode fibers are placed on a V-groove array to ensure unique fringe frequencies for each beam pair. Finally, the light from each beam is split by a polarizing beam splitter: 50% is transmitted and focused onto the fringing camera, which records the interferograms, and 50% is reflected by the polarizing beam splitter and focused onto the photometric camera, which monitors real-time fluxes of each beam for visibility and triple amplitude calibration.

into linear arrangement with equal spacing, and imaged onto a EMCCD to monitor the fluxes of each beam in real-time (the "photometric camera" hereafter). The polarization of the light perpendicular to the optical bench is imaged onto an identical EMCCD to form 15 unique sets of fringes (the "fringing camera" hereafter). The EMCCDs feature sub-electron, but non-negligible, effective read noise. Light is spectrally dispersed using identical optical (570–850 nm) slit spectrographs attached to photometric and fringing cameras. Each spectrograph has a low resolution ($R \approx 200$) and medium resolution ($R \approx 1000$) option. Below is a sequential description of each optical system, in order from the siderostats where light is collected to the EMCCD detectors:

1. *Light gathering.* NPOI uses a 12.5 cm circular beam of starlight gathered by 50 cm siderostats. The light is guided to the central beam combining facility in vacuum pipes that include 125:35 beam reducers. After beam reduction, the light is passed to delay line carts with mirrors that receive feedback from the VISION fringe tracker to match optical path lengths. The result is six coherently phased, collimated circular beams of light with 35 mm diameters.
2. *Routing light to the VISION optical bench.* The routing of the six 35 mm collimated beams from NPOI delay lines to the optical bench is shown in Figure 3. The 35 mm beams are reflected by six UV fused silica broadband plate $\frac{70}{20}$ beam splitters placed at a 45° angle to each beam (top panel, Figure 3). Some light is lost in transmission and scattering through our custom made broadband beam splitters which results in the ≈70 reflectivity and ≈20 transmissivity across 570–850 nm. The $\frac{70}{20}$ beam splitter reflects 70% of the light to VISION and transmits ≈20% of the light to NPOI's tip/tilt quad cells. The six beams are then reflected to the optical bench via 3-inch flat Newport Zerodur Broadband Metallic Mirrors with silver coating.[11] The 3-inch flat mirrors are placed 45° to the beam (bottom panel, Figure 3). At the front of the VISION optical bench are shutters that can be controlled either manually or by computer. These can block light for individual beams (panel 1, Figure 2). The six beams are then reflected off 2-inch flat mirrors to the VISION off-axis parabolas.

[11] http://www.newport.com/Broadband-Metallic-Mirrors/141088/1033/info.aspx#tab_Specifications

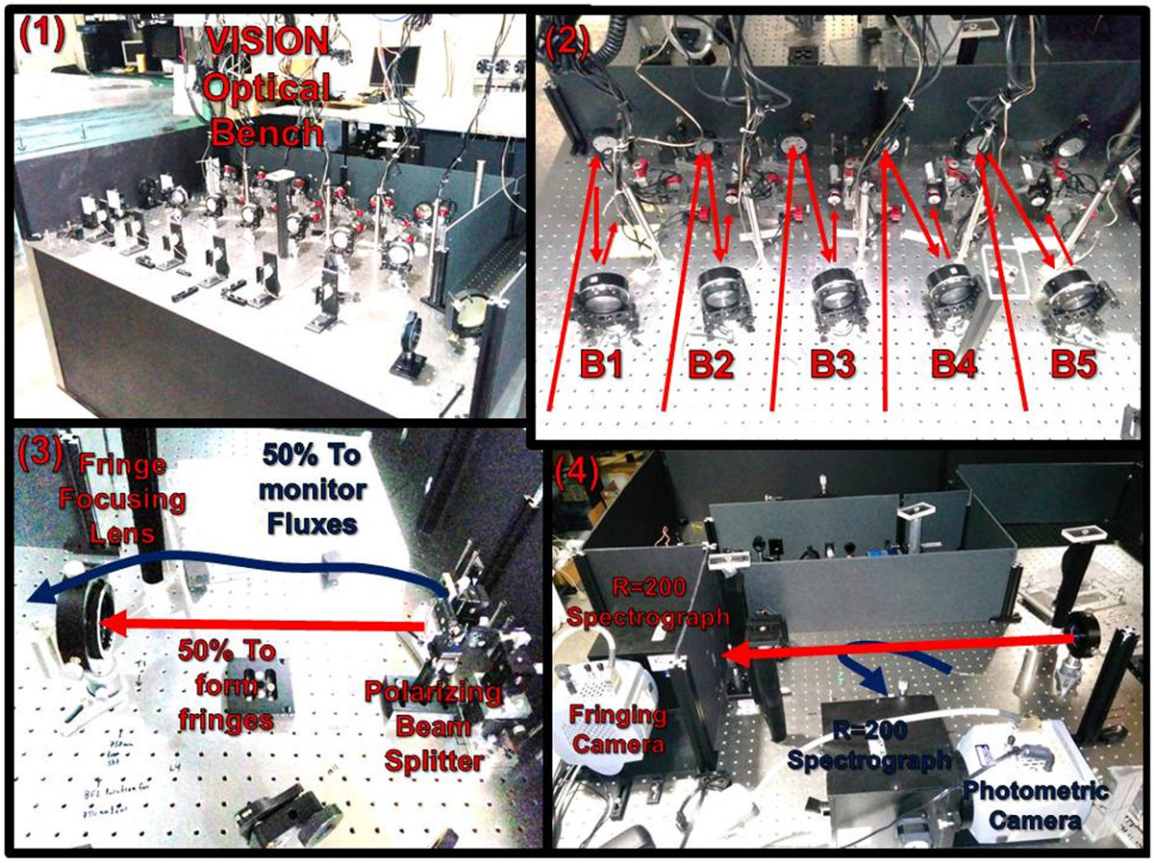

Figure 2. The light path through the VISION beam combiner. (1) The entire VISION optical bench. (2) Each 35 mm diameter beam is collapsed to a 4–8 μm spot size, focused onto each single-mode fiber tip held in place by a fiber positioner. (3) The light from each single-mode fiber is positioned on a V-groove array, where 50% is sent to the photometric camera via multi-mode fibers and 50% is sent to the fringing camera after passing through a fringe focusing lens and cylindrical lens. The photometric and fringing cameras and the identical $R = 200$ spectrographs attached to these cameras are shown in (4).

3. *Coupling light to single-mode fibers.* Each 35 mm beam is coupled to a single-mode polarization-maintaining fiber using 2-inch Nu-tek 480–900 nm silver coated off-axis parabolas (OAPs). The 165 mm focal lengths of the OAPs ($f/4.7$ optics) were calculated by Ghasempour et al. (2012) for typical $r_0 = 9$ cm site seeing using the method of Shaklan & Roddier (1988) (panel 2, Figure 2). The OAPs collapse the beams from 35 mm to 4–8 μm over 165 mm. Newport closed-loop picomotors and drivers are used to move the fibers vertically and horizontally relative to the VISION optical bench to maximize the coupling efficiency of the starlight into each fiber. This alignment is both manually and computer controllable. Except for the *X*-axis of the beam 5 driver and all of the beam 6 drivers, the picomotor drivers operate in closed-loop mode, which corrects for fiber positioning hysteresis. The fibers can be positioned to better than 2 μm, and the *X* and *Y* axis of the fibers can be aligned using an automated fiber alignment algorithm written in C++ and Python. The Newport picomotors and drivers occasionally fail with error status on startup; the picomotor drivers often require restarting a few times until they operate normally. This is an issue that will eventually be addressed but does not significantly affect performance.
4. *Single-mode polarization-maintaining fibers.* In order to increase fringe contrast, VISION uses single-mode fibers that filter the atmospheric turbulence, removing residual wavefront errors for each beam. VISION uses Nufern PM630-HP single-mode polarization maintaining fibers that are operational over 570–900 nm. The fibers are multimode at wavelengths $\lesssim$570 nm. The single-mode fibers spatially filter wavefront errors by transmitting only the fundamental transverse mode of incoming light (LP_{01}). This filtering enhances fringe contrast by partially removing spatial but not temporal atmospheric turbulence. The polarization of starlight through the fibers is maintained via strong birefringence due to stress rods

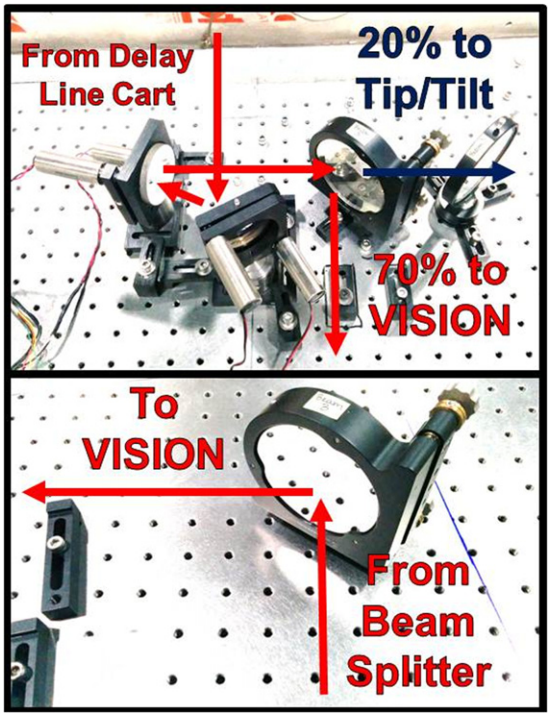

Figure 3. The light path toward the VISION beam combiner. (Top) A minority (20%) of the light passes through the beam splitter in transmission to the tip/tilt mirrors for 1st order correction of the atmospheric turbulence. The majority (70%) of the light is reflected toward VISION. (Bottom) The light is re-routed toward the VISION beam combiner.

along the slow axis of the fiber. The mode field diameter of the fibers is 4.5 μm at 630 nm, with a core size of 3.5 μm and numerical aperture of 0.12. The beam exiting each single mode fiber can be described by a Gaussian model.

5. *Non-redundant spacing with V-groove array.* VISION produces a unique fringe frequency for each telescope pair by arranging the outputs of the fibers in a non-redundant linear pattern on a silicon OZ-optics V-groove array (Table 1). The V-groove array has a base spacing of 250 μm. Non redundant fiber positions of 0-2-8-13-17-20 were chosen. After passing the light through a lens with long focal length, interference fringes are imaged. The fringe frequency, or number of pixels per fringe is:

$$\frac{\text{Pixels}}{\text{Fringe}} = \frac{f\lambda}{p(d_A - d_B)} \quad (1)$$

where λ is the wavelength of the fringe, d_A and d_B are the location of fiber A and B on the V-groove array, f is the focal length ($f = 750$ mm), and $p = 24$ μm is the size of the pixels of the camera on which the fringes are formed. Given that each fiber pair AB has a unique physical separation $d_A - d_B$ on the V-groove array, the corresponding telescope pair have a unique fringe frequency on the VISION cameras and therefore each of VISION's 15 telescope pairs has a unique signature in a power spectrum of the image (Figure 4). The VISION geometry minimizes the overlap between the peaks in power spectra for each telescope pair (the "fringe cross talk"). The fast axis of all fibers on output of the V-groove array are aligned vertically. A lenslet array glued to the polarizing beam splitter re-collimates the beams to 250 μm diameter after they exit the fibers.

6. *Output to photometric and fringing cameras.* VISION splits the light between a camera to record interferograms (the "fringing" camera), and a camera to record individual beam fluxes (the "photometric" camera), using a polarizing beam splitter. The polarization of the six beams parallel to the optical bench is reflected through the beam splitter at 90° and is coupled to six multimode fibers positioned on a second V-groove array (blue arrow, panel 3, Figure 2). It is then guided to the spectrograph attached the photometric camera (blue arrow, Figure 2, panel 4). Each beam output has a unique spatial location on the photometric camera due to a V-groove array that positions the multi-mode output for each fiber onto the photometric camera. The photometric camera monitors the real-time wavelength-dependent flux of each beam. The polarization of the light perpendicular to the optical bench is transmitted directly through the polarizing beam splitter (red arrow, panel 3, Figure 2), and is focused by a 750 mm focal length Thorlabs antireflection coated achromatic cemented doublet to a ~3.5 mm diameter spot size. Next, to condense the image in the non-fringing direction, VISION uses a 50 mm focal length cylindrical lens to collapse the light in the horizontal direction (red arrow, panel 4, Figure 2) to 24 μm, the size of a single pixel on the EMCCDs. This results in an image 24 μm by

Table 1
Laser Fringe Results

Beam Pair	Pixels Per Fringe	Fitted Visibility
1–3	39.38	0.968 ± 0.006
2–4	16.52	0.969 ± 0.010
1–4	13.89	0.939 ± 0.009
2–5	11.91	0.949 ± 0.019
3–4	10.45	0.954 ± 0.010
1–2	7.64	0.922 ± 0.005
4–5	7.01	0.884 ± 0.018
2–3	6.48	0.928 ± 0.008
1–5	4.65	0.858 ± 0.015
3–5	4.20	0.867 ± 0.014

Note. Pixels per fringe and raw visibility derived from the model fits to the 632.8 nm HeNe laser fringes in Figure 8.

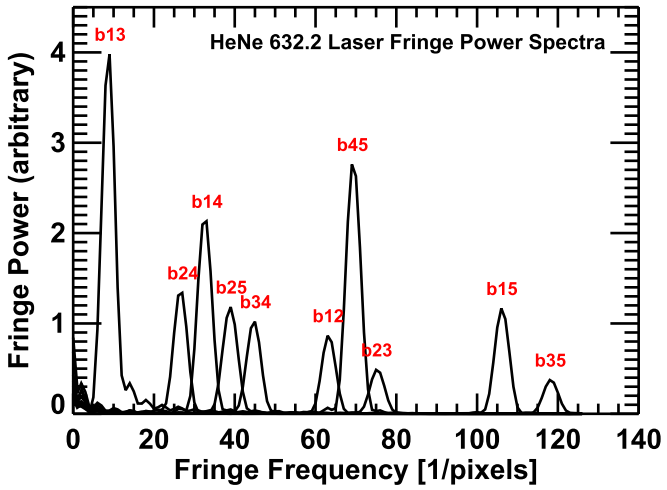

Figure 4. The unique fringe frequencies for each beam pair combination for beams 1–5 for VISION as measured using an in-laboratory 632.8 nm HeNe laser source. At fixed wavelength, the fringe frequency increases with increased distance between the fibers on the V-groove array. The peaks in the power spectra for each beam pair are well isolated resulting in very low cross talk between the fringes. The label bAB is the power spectrum peak for a fringe resulting from combining beams A and B.

3.5 mm, with fringing in the long direction that is passed to a spectrograph attached to the fringing camera, which in turn results in 128 unique spectral channels of fringes with a height of 3.5 mm in the fringing direction. The combination of the microlensarray, polarizing beam splitter, and 750 mm achromatic cemented doublet achieve the desired overlap of the six Gaussian beam profiles from the six single-mode fibers along the fringing direction on the VISION camera, which produces the fringes (see the fringe forming lens to cylindrical lens ray tracing in Figure 1). The fringes are produced at the entrance to the slit of the spectrograph.

7. *Spectrographs.* VISION spectrally disperses the incoming light using two identical Princeton Instruments SP-2156 Acton spectrographs, attached to the fringing and photometric cameras. The spectrographs are 1:1, i.e., there is no magnification of the Gaussian beam profiles at the entrance to the slit. VISION has two observing modes, one low resolution ($R = 200$) and one medium resolution ($R = 1000$). Switching between the $R = 200$ and $R = 1000$ grating for each spectrometer is remotely controllable and can be accomplished in a few seconds. The wavelength solution for the spectrographs was initialy derived using a Ne–Ar lamp source. This wavelength solution was verified with the pixel locations of the Hα feature from on-sky observations of Vega, and an in-lab HeNe laser source on the fringing and photometric cameras. The resulting wavelength solution for the $R = 200$ mode is:

$$\lambda(i) = (\lambda_{\rm cent} - 232.294) + 2.91(i + 1) - 1.30 \text{ nm, fringing camera}$$

$$\lambda(i) = (\lambda_{\rm cent} - 214.986) + 2.91(i + 1) + 4.66 \text{ nm, photometric camera}$$

where $i = 0$–127 is the pixel number, $\lambda_{\rm cent}$ is the user-chosen central wavelength of the spectrograph in nanometers, and $\lambda(i)$ is the wavelength in nanometers corresponding to pixel i. In this paper, only the commissioning of the low resolution observing mode is described, as the medium resolution mode has not yet been fully tested on sky.

8. *Andor Ixon EMCCDs.* VISION features two identical 128 × 128 pixel Andor Ixon DU 860 EMCCDs, with 24 μm square pixels and quantum efficiencies of 70%–85% over 550–850 nm at −50°C and dark current of 0.002 electrons pixel^{-1} s^{-1}. For recording stellar interferograms, the EMCCDs are operated at −50°C, with 6 ms exposure times, electron multiplying gains of 300, and fast readout rates of 10 MHz with vertical clock speeds of 0.1 μs to minimize clock induced charge (CIC) noise. The typical CIC event rate for the Andor Ixon EMCCDs was found to be 0.08–0.11 events pixel^{-1} frame^{-1}. Longer exposure times of 10–12 ms were tested on sky resulting in interferograms with significantly reduced fringe contrast due to atmospheric turbulence. Custom C++ and Python code controls data acquisition, the fringe searching, the fringe tracking, the spectrographs, the shutters, and the single-mode fiber positioners using a computer running Ubuntu Linux OS 12.04.

2.2. Raw Interferograms and Calibration Data

VISION requires large amounts of support measurements to calibrate the raw interferograms of a given star. A complete VISION data set for extracting photometrically calibrated visibilities and closure phases is shown in Figure 5 for beams 1 and 4. For both the fringing and photometric cameras, the spatial direction is vertical in the figure, and the wavelength direction is horizontal.

A sample averaged interferogram is shown in the top center panel of Figure 5 from the combined light of beams 1 and 4 using a laboratory white-light source. To produce the interferogram, the light path length difference between beams 1 and 4 was minimized using the delay line carts. The averaged interferogram was constructed from several hundred co-added, dark subtracted, 20 ms frames with a gain of 300 in medium ($R \sim 1000$) resolution mode. The low resolution observing mode is not typically used for measurements illuminated by internal light sources because the laboratory light source path passes through the $\frac{70}{20}$ beam splitters in transmission, leading to

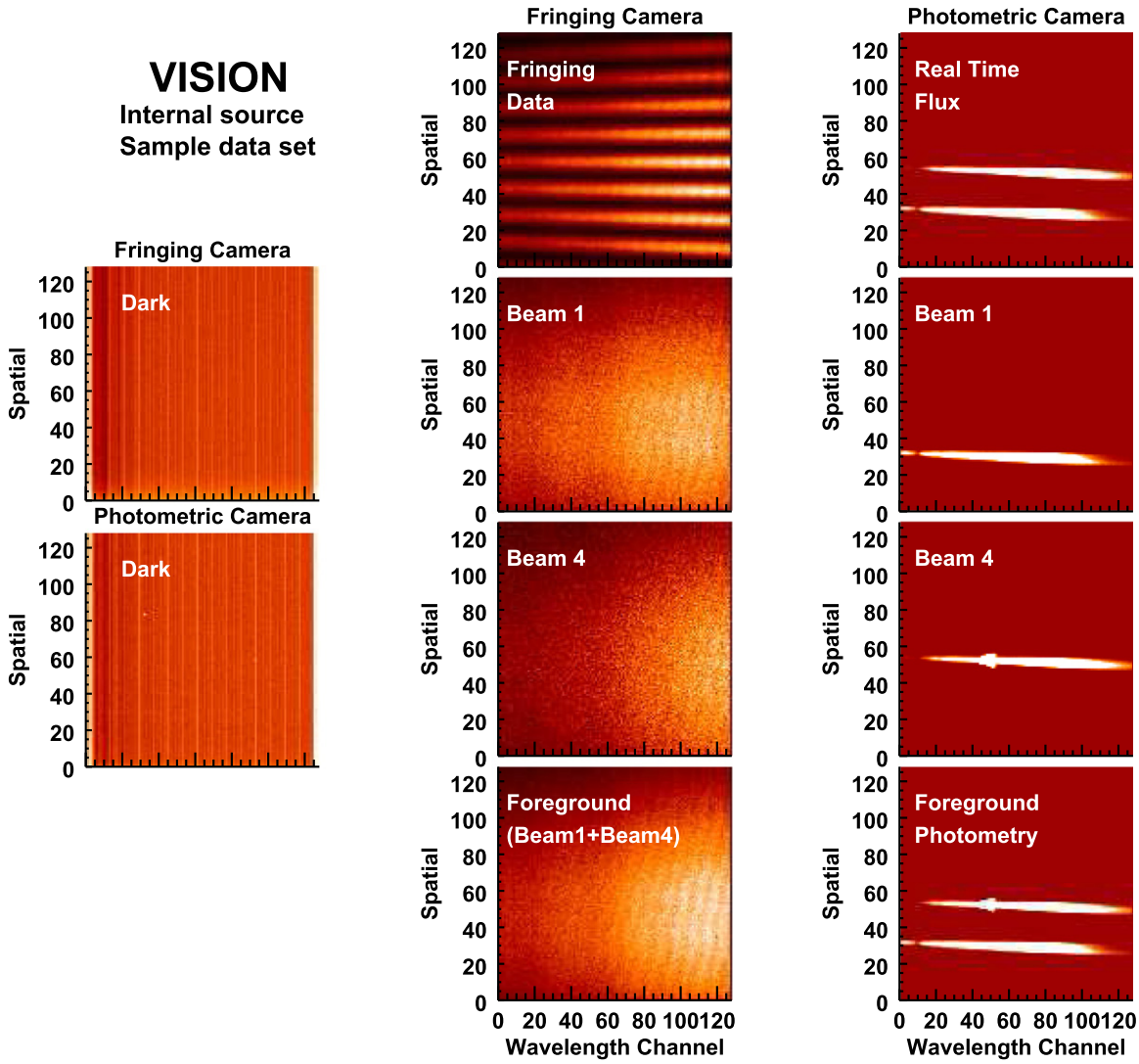

Figure 5. Sample VISION data set using an laboratory white light source with an $R = 1000$ spectrograph. A complete VISION data set to measure visibilities and closure phases includes (1) an average dark frame for both the fringing and photometric cameras to characterize the bias count structure across the EMCCDs, (2) the fringing data and simultaneous real-time flux measurements, (3) frames with light from each beam individually on the fringing and photometric cameras to measure the split of the light from the polarizing beam splitter, and (4) the foreground data to characterize the bias in the power spectrum (visibility bias) and the bispectrum. The small fringing seen in the foreground data is due to pixel-to-pixel sensitivity of the EMCCD chips. This pixel-to-pixel sensitivity only appears strongly after averaging at least 10 minutes of frames. The small point sources of light on the photometric camera frames are due to leakage of the laser metrology used by the delay line carts onto the EMCCDs.

significant dispersion. The different types of data necessary to extract calibrated squared visibilities and closure phases from any given set of interferograms are:

1. *Darks* are frames with no starlight on the detector. For each data set, $\approx 5 \times 10^3$–10^4 six-ms dark frames are recorded (requiring 30–60 s of real time). Darks are recorded by blocking incoming starlight by closing all shutters at the front of the VISION optical bench. Darks are recorded semi-hourly throughout the night for typical observing to carefully characterize the CIC and bias count levels. The sky background is not included in the darks, as it is not a significant source of photons given that VISION observes bright ($R_{\rm mag} < 4$) stars. Darks are used to estimate the EMCCD read noise, gain, and CIC rate, which are necessary parameters for extracting calibrated squared visibilities, bias-corrected closure phases, and triple amplitudes from raw interferograms. Sample average dark frames are shown in the left panels of Figure 5 for the fringing and photometric cameras.

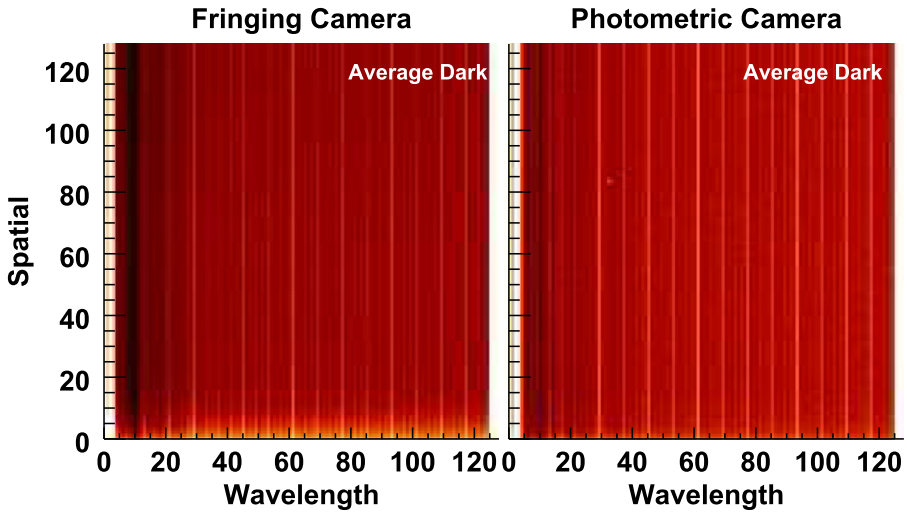

Figure 6. Thirty second time-averaged darks on the fringing and photometric cameras. There are variable bias counts across each EMCCD that must be subtracted off for each VISION data set. The maximum, median, and minimum for the average fringing camera dark are ≈87, ≈91 and ≈107 counts respectively. The maximum, median, and minimum for the average photometric camera dark are ≈97, ≈99 and ≈109 counts respectively.

2. *Foregrounds* are frames with incoherent light from all beams on the detector. Incoherent light is obtained when the delay line carts are moved many coherence lengths away from the fringing position. A sample foreground for beams 1 and 4 is shown in the bottom-center panel of Figure 5. Foregrounds are used to characterize the Gaussian profiles from the single-mode fibers on the fringing camera. This is needed to compute the power spectrum and bispectrum biases, which are in turn needed for calibrating squared visibilities and triple amplitudes.
3. *Real-time flux estimation.* The flux for each beam is recorded simultaneously with the interferograms. A sample image from the photometric camera with beams 1 and 4 is shown in the bottom right and top right panels of Figure 5.The real-time flux is used to estimate the system visibility due to beam intensity mismatch. The photometric imbalance between two beams with intensities I_A, I_B will reduce the visibility by $\frac{2\sqrt{I_A I_B}}{I_A + I_B}$ (Coudé du Foresto et al. 1997). The fringing camera beam fluxes $I_{f,A}$ and $I_{f,B}$ are estimated from the photometric camera beam fluxes, as described next.
4. *Single telescope data.* A sample set of single telescope data for beams 1 and 4 is shown in the center panels of Figure 5. The precise ratio of fluxes between the fringing and photometric cameras using the polarizing beam splitter can deviate from an exact $\frac{50}{50}$ split. This is the result of slightly varying polarization of light from the several telescopes, which is due to the siderostats' motions when tracking stars. Thus, the fringing-to-photometric light flux ratio can vary from star to star and night to night at different wavelengths. In order to calibrate this effect, the time and wavelength dependent flux ratio $\alpha(\lambda)$ between the fringing and photometric cameras are measured for each beam and for each star observed. This flux ratio is then used to correlate the real-time flux for each beam on the photometric camera to the fringing camera. The flux for each beam on the fringing camera is given as:

$$I_{f,i}(\lambda, t) = \alpha_i(\lambda, t) I_{p,i}(\lambda, t). \quad (2)$$

$I_{f,i}(\lambda, t)$ is the flux at wavelength λ and time t on the fringing camera for beam i, and $\alpha_i(\lambda, t)$ is the measured wavelength- and time-dependent flux ratio between the fringing and photometric cameras using single beam data for beam i:

$$\alpha_i(\lambda) = \frac{I_{f,i}(\lambda)}{I_{p,i}(\lambda)} \quad (3)$$

where the fringing-to-photometric camera flux ratio $\alpha_i(\lambda)$ is measured using single beam data (center panels, Figure 5). Equations (2) and (3) are used to estimate the flux on the fringing camera for each beam, i, separately. The estimated fluxes for each beam on the fringing camera are used to correct observed squared visibilities and triple amplitudes for beam intensity mismatch.

2.3. Daily Alignments

A series of daily alignments are performed for each of the six beams to maximize the starlight throughput for on-sky observations, using a 632.8 nm HeNe laser source. The procedure is as follows:

1. Align the "switchyard" mirror (top panel, second mirror in the light path of Figure 3) to the $\frac{70}{20}$ beam splitters in order to route each beam toward the VISION "switchyard" table.
2. Mount the $\frac{70}{20}$ beam splitters and accompanying beam-shear compensating windows. The beam splitters route light from the feed system to the VISION optical bench.
3. Place an auto-collimation mirror directly in front of each of the $\frac{70}{20}$ beam splitters, thus retro-reflecting the HeNe laser back on itself and to the VISION optical bench. This is necessary because the HeNe laser light path is opposite that of the feed system.
4. Align the $\frac{70}{20}$ beam splitters (top panel, Figure 3) to place the laser spot as close as possible to the fiber tip of each single-mode fiber.
5. Align each fiber with an automated algorithm that directs the fiber to move horizontally and vertically to the optical bench until the laser light coupled to the fiber is at maximum. This alignment algorithm typically is repeated twice, once as a rough pass with total grid search size of $32 \times 32\ \mu$m, and once with a smaller grid search size of $8 \times 8\ \mu$m. Occasionally, the fiber focus for each beam is determined using the fiber alignment algorithm.
6. Remove the auto-collimation mirrors, and after acquiring a star, re-align the fibers to maximize the coupling of starlight to each fiber.

3. Data Acquisition

3.1. Fringe Searching

The fringe search algorithm acquires fringes by automatically stepping the delay line carts back and forth until the fringes are found. For the first star observed each night, this procedure typically takes several minutes. After that, offsets of 1–3 mm in the cart positions generally remain fixed throughout the night, and the fringe searching on subsequent stars can take less than a few seconds. VISION takes advantage of the roughly equal spacing of the NPOI array to use the shortest baselines to phase the long baselines via baseline bootstrapping (Armstrong et al. 1998a; Jorgensen et al. 2006). The fringe search algorithm uses up to 5 baselines for fringe searching and fringe tracking. For single stars that are resolved with NPOI baselines, the shortest baselines are typically used to fringe search, since the visibility is highest on the first peak of the visibility function. For binary stars, the baselines used for fringe tracking are strategically chosen based on the observed fringe SNR on each baseline, and this can be done in real time.

For example, for 3-way beam combination on a star using beams 2, 4, and 5, beam pairs 2–4 and 4–5 can be selected for fringe tracking while the longer baseline with beam pair 2–5 is also phased without additional delay line feedback. Each of the fringe searching and fringe tracking parameters are adjustable.

Next the fringe search algorithm is detailed for beams 2, 4, and 5 with the nominal settings:

1. First, the algorithm begins searching for fringes between beams 2 and 4 with an increasing search pattern around the nominal delay point, stepping delay line cart 4 by $\sim+20\ \mu$m. If the fringe SNR is greater than the semi-lock SNR at least $\sim$3 consecutive times, then the fringe is considered "found." The fringe SNR is estimated in the control system code after the sum of $\sim$20 power spectra co-adds:

$$\mathrm{SNR} = \frac{\text{Peak of power spectrum}}{\text{Average power spectrum noise}}. \quad (4)$$

   If the fringe is not found by the time the delay line cart has reached $\sim$500 μm, the cart stepping reverses direction with steps of $\sim-20\ \mu$m until the cart has reached $\sim-500\ \mu$m.
2. If no fringe is found, the search range is repeated and increased by $\sim2\times$, from ~-1000 to $+\sim1000\ \mu$m about the nominal delay point. This search range is increased continually until the fringe is found, which is typically within 1–3 mm of the nominal delay point for the first star observed that night.
3. Once the fringe is found, if the fringe SNR is greater than the track SNR, tracking begins on beam pair 2–4, with delay line feedback sent to cart 4 to correct for atmospheric piston errors. If the fringe SNR is lower than a separate "fringe-lost" SNR at least $\sim$3 times, then the fringe searching for cart 4 resumes, with a small, fixed delay range of $\pm\sim5\ \mu$m.
4. The fringe search algorithm then repeats the above process to search for fringes between beams 4 and 5. Searching for fringes using delay line cart 5 is relative to any delay line feedback sent to cart 4. The fringe search algorithm automatically keeps the cart of the first beam given as the stationary cart. In this example, the algorithm was given tracking beam pairs 2–4 and 4–5 and thus cart 2 was kept stationary. If the algorithm is tracking beam pairs 4–2 and 2–5, it would keep cart 4 stationary.

3.2. Fringe Tracking

Due to atmospheric turbulence, the path length that light travels from each star to the telescopes often changes on 10–500 ms timescales. To correct for this effect the fringes are tracked in real time using a fringe tracking algorithm. The fringe tracking code is written in C++ and installed on the VISION control system computer, which sends feedback directly to the delay line carts.

VISION forms spatially dispersed fringes on the fringing camera in real time, and thus avoids the need for modulation of the delay line mirrors to create temporal fringes. This design was chosen to avoid possible nonlinear modulations in the shapes of the delay line modulations observed in NPOI classic, which can lead to cross talk between the fringe amplitudes and phases, when multiple baselines are observed with the same detector pixel.

A fringe-fitting approach is used to estimate group delay in the fringe tracking algorithm. The delay to move each of the five operational delay line carts is evaluated on ≈100 ms timescales to minimize the path length differences between the carts, ideally to within a few hundred nm or better. The fringe tracking approach uses a Fourier transform along the wavelength direction, and a direct fit to the data along the fringing (spatial) direction for each 6 ms frame of data. The theoretical fringe model for an image plane combiner adopted from Equation (10.1) on page 569 of Born & Wolf (1999) is:

$$I(y) = I_1 + I_2 + 2\sqrt{I_1 I_2}|\gamma|\cos(fy + \arg(\gamma)) \quad (5)$$

where, I_1 and I_2 are the fluxes for beams 1 and 2 respectively. The coherence between the two beams γ has both an amplitude $|\gamma|$ and a phase arg (γ), and the fringes are modulated by frequency f. Note that the phase can be instead represented by replacing the cosine function with independent cosine and sine functions each with independent amplitudes using the identity

$$\cos(\theta_1 - \theta_2) = \cos(\theta_1)\cos(\theta_2) + \sin(\theta_1)\sin(\theta_2);$$

the phase would be found as the inverse tangent of the ratio of sine to cosine amplitudes. This allows the nonlinear phase parameter to be replaced by linear coefficients, simplifying model fitting procedures.

If only a single telescope pair were being used, and if there were no further modulation of the fringe amplitude, the intensity pattern could be fit using a Fourier Transform, and implemented efficiently in real time using, for example, the Fast Fourier Transform algorithm (with attention to zero-pad the array for better sampling of the fringe frequencies f, since the fringe wavelengths will not necessary be integer fractions of the number of pixels).

In practice this theoretical fringe model is modulated by both a coherence envelope (as a function of distance from zero differential optical path length) and detector illumination pattern, and multiple fringe signals are present simultaneously. The first can be modeled according to the instrument and source bandpasses (though only with nonlinear parameters), and the second according to incoherent illumination pattern measurements. For fringe tracking, a model combining the effects of the illumination pattern and fringing is used as follows (however, the coherence envelope is presently ignored in real-time analysis due to nonlinear parameter complexities).

Fringes are dispersed horizontally (x), with the fringing (delay) direction vertical (y). For a given spectral channel x, the interferogram is modeled as

$$I(x, y) = e^{-(y-P_1)^2/P_2^2} \times \left(P_3 + \sum_{k=1} [P_{4,k}\cos(P_{6,x,k}(y - 64 - P_{7,x,k})) + P_{5,k}\sin(P_{6,x,k}(y - 64 - P_{7,x,k}))] \right) \quad (6)$$

where k is the index of each beam pair, P_1 and P_2 describe the approximately Gaussian illumination pattern on the detector, P_3 is the overall intensity, $P_{4,k}$ and $P_{5,k}$ are the cosine and sine amplitudes for each pair (with the phase ϕ given by $\tan\phi = P_{5,k}/P_{4,k}$ and the total fringe amplitude $\sqrt{P_{4,k}^2 + P_{5,k}^2}$), and $P_{6,x,k}$ is the (wavelength dependent) fringe frequency. More generally, the form can be written as

$$I(y) = \sum_{m=0}^{m=2N} A_m g_m$$

where

$$g_m(x, y) = \begin{cases} 1 & m = 0 \\ e^{-(y-P_1)^2/P_2^2}\cos \times(P_{6,x,k}(y - 64 - P_{7,x,k})) & m = 2n - 1,\ m \text{ odd} \\ e^{-(y-P_1)^2/P_2^2}\sin \times(P_{6,x,k}(y - 64 - P_{7,x,k})) & m = 2n,\ m \text{ even} \end{cases}$$

and these functions can be precomputed based on laboratory evaluations of the Gaussian profile parameters P_1 and P_2, fringe frequencies $P_{6,x,k}$, and internal differential dispersion $P_{7,x,k}$ (presently set to zero). The remaining coefficients A_m are all linear, allowing for a single matrix inversion to solve the best χ^2 fit. This is efficient to implement in real-time, whereas an iterative nonlinear fitting procedure would be prohibitively slow. It is also trivial to parallelize the fit computations, as each spectral channel's fit is evaluated independently.

The typical fringe tracking parameters are given in Table 4 and are optimized with on-sky observations in median seeing conditions. An exposure time of 6 ms is commonly used for the EMCCD. The typical fringe search step sizes are ∼12.5 μm. During fringe tracking, two 6 ms frames are added together for a total on-sky coherent integration time of 12 ms (2 coherent co-adds). While a 12 ms effective exposure time on sky does reduce the fringe SNR (see Equation (4) in Section 3.1) due to the atmospheric fluctuations, the added flux more than makes up for the lost fringe SNR. Fringe fitting is done as described above using Equation (6) to determine P_4 and P_5. The group

Table 2
Observing Sequence

Align Fibers	120 s
Take Darks	30 s
Fringe Search	30 s
Record Fringes	720 s
Record Foreground	60 s
Record Single Beams 1−6	45 s per beam
Total	1230 s

Note. The observing sequence for each target or calibrator star. Raw interferograms are recorded while fringe tracking. The fibers only need to be aligned a couple of times per night. The rest of the data obtained are used to calibrate these raw interferograms: "Dark" frames are used to subtract off the bias counts of the EMCCDs. "Foreground" frames are observations of the star with incoherent flux (no fringes). These data are used to characterize the bias in power spectrum and triple amplitudes. "Single Beam" frames are the flux measurements of each beam individually, which is used to measure how the polarizing beam splitter splits light between the photometric and fringing cameras at each wavelength.

delay for each telescope pair is estimated by treating P_4 and P_5 as the real and imaginary components of a 1D Fourier Transform (FT) for that frequency, and another 1D FT along the wavelength direction using the FFTW[12] program in C++ (Frigo & Johnson 2005) is performed. The resulting power spectrum is coadded over thirty 12 ms co-added frames, for an effective in-coherent exposure time of 360 ms (30 incoherent co-adds) to generate a total power spectrum. The location of the peak of the total power spectrum corresponds to the delay that is sent to the delay line carts.

3.3. Observing Sequence

A complete observing sequence for a target or calibrator star is detailed in Table 2. After acquiring the star, the fibers are aligned to maximize the light coupled using an automatic fiber alignment algorithm. This step is typically required several times a night depending upon whether the observed fluxes are lower than expected. Next the different types of VISION data necessary to calibrate the observed interferograms in post-processing are recorded: darks, interferograms while fringe tracking, foregrounds, and single beam data, as detailed in Section 2.2.

Target star and calibrator star observation sequences are interleaved. Calibrator stars are selected that are typically 1–4 mas (depending upon whether longer (30–80 m) or shorter (8–12 m) baselines are used) to correct for the system visibility drift and bispectrum bias in the data. For typical ≈2 hr observations of a given star, a calibrator-target-calibrator pattern is alternated on ≈20 minutes timescales, given that single beam and foreground data are required. A typical VISION observation of a star produces 20–50 GB of raw data, and consists of $\approx 10^6$ individual frames with 6 ms exposures; an observing run typically produces 200–400 GB of raw data per night.

3.4. Faint Magnitude Limit

Fringe detection has been demonstrated with current hardware at apparent magnitude $R_{\rm mag} = 4.5$, in excellent seeing. Funds from the Office of Naval Research DURIP competition have recently been received to replace the existing Andor DU-860 EMCCDs used for fringe detection and intensity mismatch monitoring with new Nüvü EMCCDs. The new EMCCDs feature ×10 less CIC noise (0.005 events pixels^{-1} per frame) as compared to our measured CIC of 0.08–0.11 events pixels^{-1} per frame. This reduced noise is expected to greatly improve our faint magnitude limit.

4. Characterizing the VISION Instrument

4.1. System Throughput

An observed throughput of 0.67% was measured using the average total flux of of γ Orionis on the night of 2015 March 16, in median seeing. The total observed photons per second $F_{\rm obs}$ for γ Orionis was estimated as:

$$F_{\rm obs}\,({\rm phot\ s^{-1}}) = \sum_{i=0}^{i=127} \frac{\pi}{4} D^2 \langle F_0 \rangle\, 10^{-0.4(R_{\rm mag}+kz)} \times \frac{\lambda_i}{hc} \Delta\lambda \langle T \rangle \quad (7)$$

where i is the pixel index on the VISION fringing and photometric cameras, $D = 12.5$ cm is the effective collecting area diameter, $k = 0.11$ is the extinction in R-band in magnitudes, $z = 1.43$ is the airmass during the observations, $\langle F_0 \rangle = 2.25 \times 10^{-9}$ erg cm^{-2} s^{-1} Å^{-1} is the zero magnitude R band flux, $R_{\rm mag} = 1.73 \pm 0.1$ (Ducati 2002) is the magnitude γ Orionis from SIMBAD[13] (Wenger et al. 2000), λ_i is wavelength of light at pixel i on the cameras, h is Planck's constant, c is the speed of light, $\Delta\lambda \approx 1860$ Å is the wavelength range over the entire filter, and finally $\langle T \rangle$ is the average throughput for the observations. $F_{\rm obs}$ for γ Orionis was measured on both the fringing and photometric cameras on 2015 March 16 in median seeing. We computed the observed throughput, for both the fringing and photometric cameras by solving Equation (7) above for $\langle T \rangle$.

Accounting for all optical surfaces from the telescopes to the beam combiner, a total theoretical throughput of ≈8.6% was computed by multiplying the reflectivity and transmission of all optical surfaces from the telescope to the VISION cameras including filter response and quantum efficiency as detailed in Table 3. The total observed throughput was ≈0.67%, which is

[12] http://www.fftw.org/

[13] http://simbad.u-strasbg.fr/simbad/

Table 3
Throughput

Reflection	
Feed System	75%
Delay Line Carts	73%
$\frac{70}{20}$ Beam Splitter, (20% to Tip/Tilt)	70%
3 Inch Flat Mirror (Protected silver coating)	96%
2 Inch Flat Mirror (Silver coating)	98%
Off Axis Parabola (Silver coating)	98%
Fiber Coupling Efficiency ($r_0 = 9$ cm)	55%
Fiber Fresnel Air-to-Glass	92%
Lenslet Array at output of Fibers	98%
Light to Fringing Camera	
Polarizing Beam Splitter *S* mode	50%
Fringe Focusing Lens (AR coating)	97%
Cylindrical Lens (AR coating)	98%
$R = 200$ Fringing Spectrograph Filter	62%
Quantum Efficiency of Andor Ixon DU 860 (8% loss from air to chip)	83%
Throughput Fringing Camera (theoretical)	≈4.2%
Throughput Fringing Camera (observed)	≈0.45%
Light to Photometric Camera	
Lenslet Array at input of Multi-mode Fibers	98%
Polarizing Beam Splitter *P* mode	50%
$R = 200$ Photometric Spectrograph Filter	62%
Quantum Efficiency of Andor Ixon DU 860 (8% loss from air to chip)	83%
Throughput Photometric Camera (theoretical)	≈4.4%
Throughput Photometric Camera (observed)	≈0.22%

Note. List of throughput for the VISION fringing and photometric cameras. Most VISION mirrors are silver-coated. The biggest single contributor to the loss of light is coupling to the single-model fibers. The theoretical fiber coupling efficiency of 55% is likely greatly over estimated due to feed alignment and delay line cart optics misalignments detailed in Section 4.1.

nearly 13 times lower than the theoretical throughput. This significant difference could be due to the adopted throughput of the NPOI feed system and the delay line carts of ≈75% and ≈73% respectively, as measured 9 years ago by Zhang et al. (2006). The loss of light in the feed system could be much larger due to 9 additional years of optical coating degradation. Similarly, the delay line cart mirrors have drifted out of focus, meaning the adopted theoretical fiber coupling efficiency of 55% is likely overestimated. An additional cause of lost light is that the fringing camera does not sample the full Gaussian profile from each fiber on the detector as shown in Figure 7, which leads to ≈30% loss in light. Finally, the misalignment of the focusing optics for light from the multi-mode fiber output to the photometric camera also could lead to an additional loss of light for beams 3 and 5, which are on the edges of the photometric camera chip.

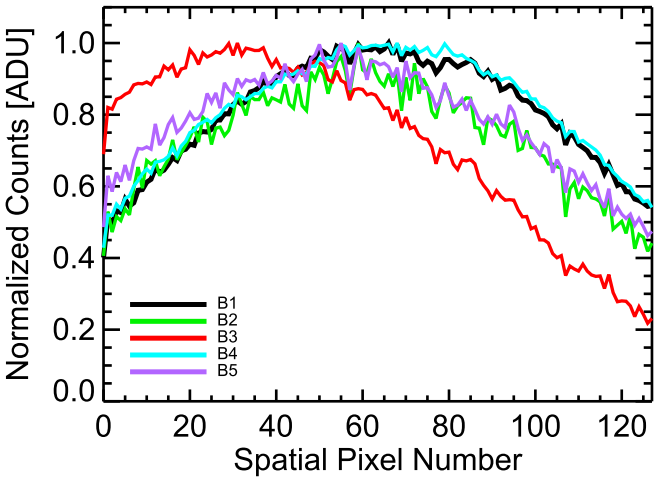

Figure 7. The wavelength averaged (550–850 nm) shape of the Gaussian beam profile outputs from the single mode fibers on the fringing camera (see Section 4.2). All five beams overlap well. A Gaussian shape is expected for the LP_{01} mode of electric field that propagates through each single-mode fiber used for VISION. Beam 3 is offset from the center of fringing camera chip due the single mode fiber being slighlty misplaced in the V-groove array.

4.2. Beam Overlap

Fringes can only exist where the Gaussian beam profiles of each single-mode fiber overlap on the fringing camera. The Gaussian beam profile was measured for each beam individually on the fringing camera using a laboratory white light source, 20 ms exposure times, a gain of 300, and the low resolution $R = 200$ observing mode. Ten minutes of frames were recorded on the fringing camera for each beam to build high-SNR Gaussian beam profiles. Figure 7 illustrates the overlap for all 5 beams averaged over 570–850 nm. With the exception of beam 3, the percent flux overlap for each beam with each other beam is >90%. The percent flux for beam 3 that overlaps with beams 1, 2, 4, and 5 is 72%–79%. The lower overlap for beam 3 is likely due to a slight misplacement of the fiber for beam 3 in the V-groove array. The lower overlap fraction in beam 3 can lead to slightly lower fringe contrast between beam 3 and the other beams. These systematic differences in visibility can be removed by observing a calibrator star.

4.3. Laboratory Fringe Model

Given that VISION uses single-mode fibers, high visibilities of >80% are expected for all beam pairs under ideal laboratory conditions, similar to commissioning tests of other beam combiners such as MIRC and AMBER (Petrov et al. 2007) that use optical fibers. This maximum possible visibility measured for a given beam pair under ideal conditions is the "system visibility." In order to verify that the system visibility is >80%, a fringe model was chosen to match sets of high signal-to-noise

laboratory fringes that do not suffer from visibility loss due to beam intensity mismatch and atmospheric turbulence or CIC noise. Equation (6) was parameterized making the basic fringe model directly comparable to VISION interferograms, at a single wavelength channel:

$$I(x, y) = e^{-(y-P_1)^2/P_2^2} \times \left(P_3 + \sum_{k=1} \frac{\sin(P_8 y + P_9)}{P_8 y + P_9} \times [P_{4,k} \cos(P_{6,x,k}(y - 63.5 - P_{5,k}))] \right) \quad (8)$$

where parameters $P_{4,k}$ and $P_{5,k}$ are redefined as overall fringe amplitude and phase, and new parameters P_8, P_9 are introduced modulation by the coherence envelope due to the finite spectral resolution of the detector, which can be modeled by integrating over several wavelengths.

The integration is done by evaluating the fringe model at 0.01 pixel steps, or 1.28×10^4 evenly spaced points from pixels 0–127, and integrating the resulting model fringe to 128 pixels. By integrating, the pixelation of each interferogram by the finite spectral resolution is modeled. The fringe model (Equation (8)) assumes a rectangular bandpass, due to the use of a sinc function. The model is an approximation given that the VISION bandpass is likely closer to a Gaussian and not square (as dictated by a sinc function) for each resolution element, but was sufficient for the present study.

The system visibilities for all 10 available beam pairs (beams 1–5) were measured under laboratory conditions using the fringe model above. The fringe parameters for each beam pair were evaluated by fitting the fringe model in Equation (8) to interferograms from a laboratory HeNe 632.8 nm laser source. The visibility was estimated as the ratio between total flux on the detector and the amplitude of the coherence:

$$V = \frac{P_4}{P_3} = 2\frac{\sqrt{I_1 I_2}}{I_1 + I_2}|\gamma|. \quad (9)$$

The procedure to obtain the interferograms for each beam pair was as follows. First, a 632.8 nm HeNe laser source was coupled to the single-mode fiber of each beam. The delay line carts were positioned to minimize light path difference between the two beams to within the coherence length ($\lesssim$1300 μm), maximizing the visibility for a given pair of beams. Several minutes of 2-ms exposure time raw interferograms were recorded for each beam pair and the gain set to zero. Electron multiplying gain was not used in order to avoid additional multiplication noise. A time averaged dark was subtracted from each of the raw interferograms to remove the bias counts on the EMCCD. A median selected dark was not used because there was negligible CIC on the detector when running the EMCCD with zero gain.

The system visibility was $V_{\rm laser} \approx 85\%$–$97\%$, as expected when using single-mode fibers. Fitting was performed using IDL's MPFIT[14] which employs a modified Levenberg-Marquardt χ^2 minimization to fit the fringe model (Equation (8)) to the interferograms. Sample interferograms for each beam and model fits are shown in Figure 8. The residuals between the fringe model and the interferograms are 1%–5% as shown in Figure 9, as expected given the imperfect fringe model (e.g., sinc envelope instead of Gaussian). Nevertheless, the laboratory system visibilities for VISION were >80% for all beam pairs, as expected.

4.4. Fringe Crosstalk

Fringe analysis based on Fourier Transforms shows slight overlap among the peaks in the power spectra from each beam pair (see Figure 4). This is because the fringes do not fit along the 128 pixels of the fringe direction an exact integer number of times. While the fringe frequencies were selected to be unique and produce orthogonal intensity pattern functions, sinusoids are only orthogonal on domains in which both sinusoids have an exact integer number of waves. (Even if a perfect integer number of waves fit across the detector for one wavelength, this would not be the case for other wavelengths.) As a result, the fringe sinusoids are not strictly orthogonal functions on the domain of 128 pixels, though they may be unique and orthogonal overall. This results in perceived cross-talk between channels even in the case of a perfect setup (instrumental alignment inaccuracies will add to the effect). This is independent of the method used to evaluate the fringe models and instead related to the non-orthogonality of the basis functions on the 128 pixel restricted domain.

As expected, the observed crosstalk between peaks in the power spectra were found to occur between pairs of beams that are closest in fringe frequency such as beam pairs 1–4 and 2–5. The crosstalk percentage was calculated as the total power in the power spectrum for each beam pair at the location of the peak of each other beam pair. The magnitude of the fringe crosstalk using the Fourier Transform method was found to be $\approx$1%–8% of the power in the power spectra for the laboratory fringes. Fringe fitting with better fringe models (including illumination profile, coherence reduction far from zero optical path delay, dispersion, etc.), as described in Section 3.2 and below, can improve but not entirely eliminate these effects.

In an attempt to further understand the crosstalk, a multi-fringe model based on Equation (8), was used to fit fringes from multiple beam pairs on the detector. Laser fringes from beam pairs 1–4 and 2–5 were added together and fit for parameters of both beam pairs simultaneously.

In Figure 11 the χ^2 space is mapped by varying the amplitude of the fringes, parameter $P_{4,k}$ for both beam pairs 1–4

[14] http://www.physics.wisc.edu/~craigm/idl/down/mpfit.pro

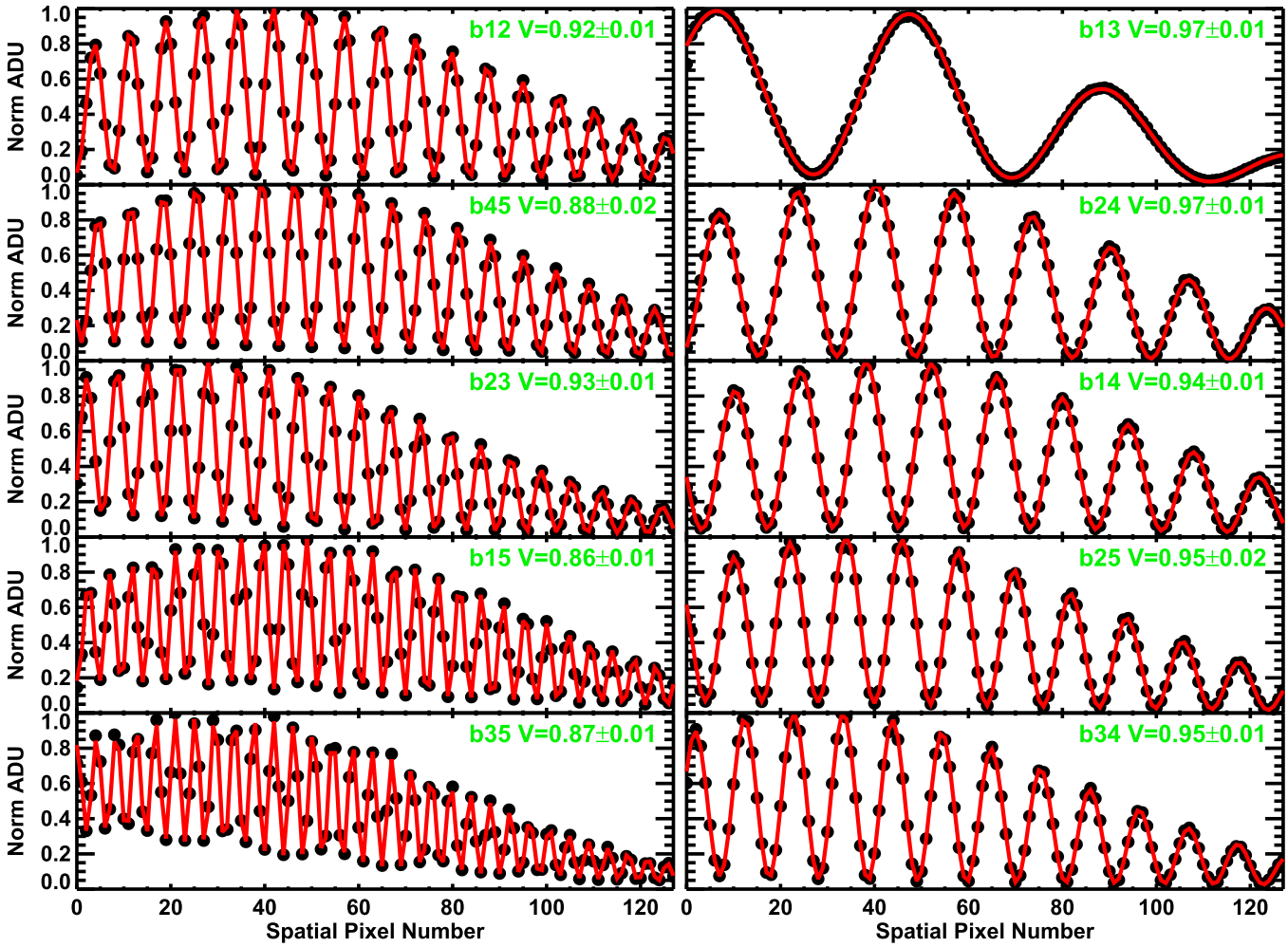

Figure 8. Interferograms using a 632.8 nm HeNe laser source and matched light paths for each beam pair for beams 1–5 (see Section 4.3). A fringe model was fit to each set of laser fringes for each beam pair using the fringe model Equation (8), and measure visibilities of 85%–97%, which implies that the majority of light is interfering. The small visibility loss could be the result of polarization effects, beam intensity mismatch.

and 2–5 in Equation (8) above. For two parameters of interest, $\Delta\chi^2 = 2.30$, 6.17, and 11.8 for 1σ, 2σ, and 3σ confidence intervals respectively (Press et al. 2002). Even for ideal, high SNR fringes, a correlation in the visibilities is seen of both beam pairs at the $\approx$2% level for the 3σ confidence interval. This could also be interpreted as a form of crosstalk. This test suggests that the χ^2 minimization between a multi-fringe model and multi-fringe data likely leads to correlations between the visibility parameters and is thus a manifestation of crosstalk, similar to the overlapping peaks in the power spectra.

5. The VISION Data-processing Pipeline

5.1. Dark Subtraction Algorithm

Dark frames are used to subtract the bias counts for all raw calibration data and interferograms. The bias counts are important to characterize given that average signal counts can be as low as $\approx$0.1 photons pixel^{-1} frame^{-1} for $R_{\rm mag} \approx 3.5$ stars. Bias level subtracted interferograms and calibration data are used in the data processing pipeline. Following Harpsøe et al. (2012) the bias count levels on the photometric and fringe camera chips were characterized by the sum of time-dependent (frame to frame) and spatially dependent bias counts:

$$b(x, y, t) = b(x, y) + b(t) \tag{10}$$

where $b(x, y, t)$ are the bias counts at pixel (x,y), and time t. Andor's "baseline clamp" software stabilizes $b(t)$ for each frame by subtracting off a running average of a 128 pixel overscan region of the chip and then adding back in 100 Analog-to-Digital Units (ADU). The output probabilities of ADU for the EMCCDs are characterized using an analytic model that is a convolution of the probability that a pixel will have a CIC event or just a bias count (Equation (8), Harpsøe et al. 2012).

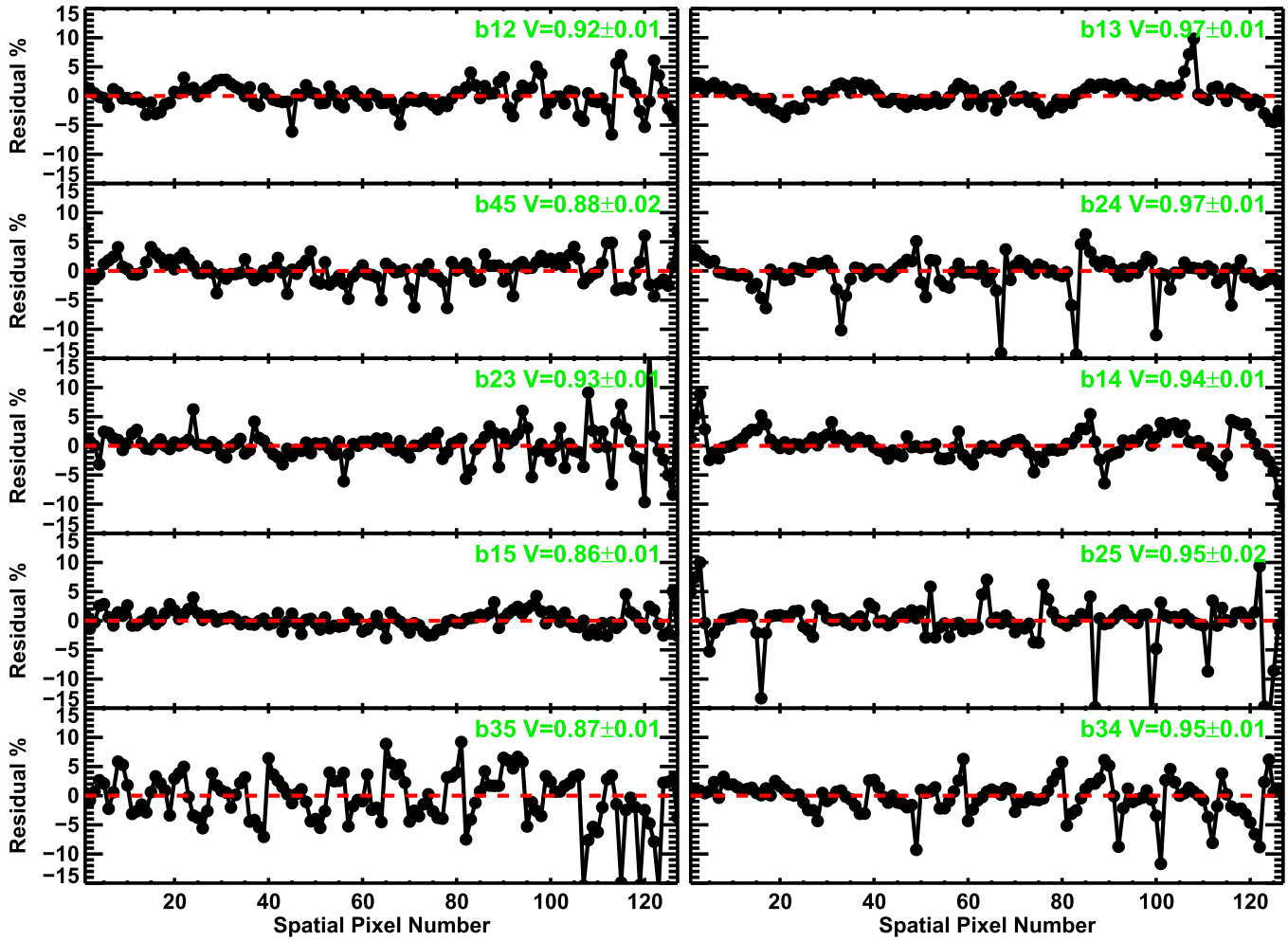

Figure 9. The residuals for Figure 8.

This analytic EMCCD model was modified to include the probability that two CIC events occur in the same pixel, given that the probability of a CIC electron is ≈8%–11% for the EMCCDs, and thus the probability of two concurrent CIC electrons was ≈0.6%–1.2%, which is significant for characterizing the high end tail of pixels with >200 ADU:

$$P(Z=n)=\int_0^n\left[(1-p-p^2)\left(\delta(x)+\left(\frac{p}{G}e^{-x/G}+\frac{p^2}{G^2}xe^{-x/G}\right)H(x)\right)\right]\times N(n-x,\sigma_{\rm RN})dx \tag{11}$$

where $P(Z=n)$ is the normalized probability that a given pixel will have output n ADU. Furthermore, p is the probability of CIC, G is the gain, $\sigma_{\rm RN}$ is the read noise in ADU, $H(x)$ is the heaviside step function, and $N(n-x,\sigma_{\rm RN})$ is the normal distribution that describes the bias counts $b(x, y)$ at each pixel:

$$N(n-x,\sigma_{\rm RN})=\frac{1}{\sqrt{2\pi\sigma_{\rm RN}^2}}e^{-(n-x)^2/(2\sigma_{\rm RN}^2)} \tag{12}$$

where $N(n-x,\sigma_{\rm RN})$ describes the bias counts (which has Gaussian read noise) when no CIC event occurs. If a CIC event occurs, the output counts n from the EMCCD go as $\frac{e^{-x/G}}{G}$ (Basden & Haniff 2004).

This EMCCD model was tested by fitting a histogram of 10^5 raw dark frames from the fringing camera on a pixel by pixel basis to derive a bias count level $b(x, y)$, read noise $\sigma_{\rm RN}(x, y)$, gain $G(x, y)$, and CIC probability $p(x, y)$. The darks were recorded with 6 ms exposures, and a gain setting of 300 on the camera. The modified Levenberg least squares minimization algorithm MPFIT (Markwardt 2009) was used to fit the EMCCD model to the darks. A sample fit to pixel $(x, y) = (50, 50)$ is shown in Figure 12. The EMCCD model

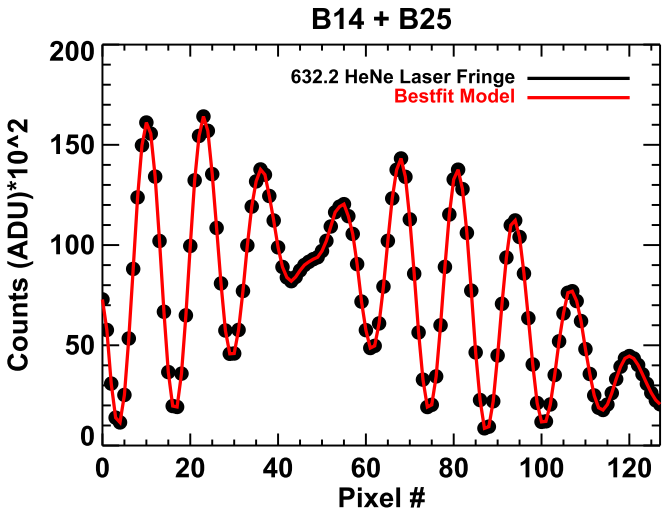

Figure 10. Laser fringe data from beam pair 1–4 and 2–5 added together on the detector, with the corresponding best fit model using Equation (6) in Section 4.4.

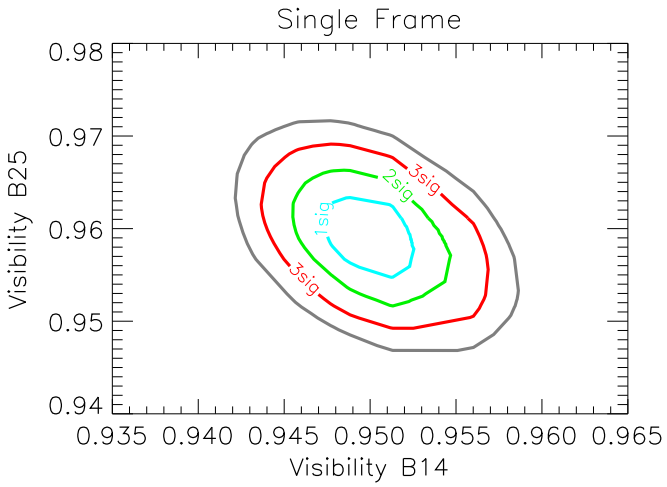

Figure 11. A map of χ^2 space for the correlation between the visibility of beam pair 1–4 and beam pair 2–5, using co-added laser fringes. The confidence intervals correspond to $\Delta\chi^2 = \chi^2 - \chi^2_{\rm min} = 2.30$, 6.17 and 11.8 for 1σ, 2σ and 3σ respectively for 2 parameters of interest (see Section 4.4, and also Press et al. 2002). The visibility parameters for either beam pair are correlated on the ≈2% level for the 3σ confidence interval even for these very high signal-to-noise laser fringes. This suggests crosstalk is inherent to the instrument set up.

fit the data well with small residuals. The typical read noise was $\sigma_{\rm RN,obs} \approx 3.5$ ADU,[15] gain of ≈16–18, and CIC probability of ≈11%–13% averaged over the entire chip for the fringing camera. The observed gain of ≈16–19 is 258–305 when multiplied by the e^-/ADU conversion of 16.3 and 16.1 for the fringing and photometric camera, respectively. This gain is

[15] Following the literature convention, counts instead of electrons are used given that the gain on an EMCCD is stochastic and varies as a function of time and location on the detector. Therefore there is no exact conversion between electrons and ADU for an EMCCD.

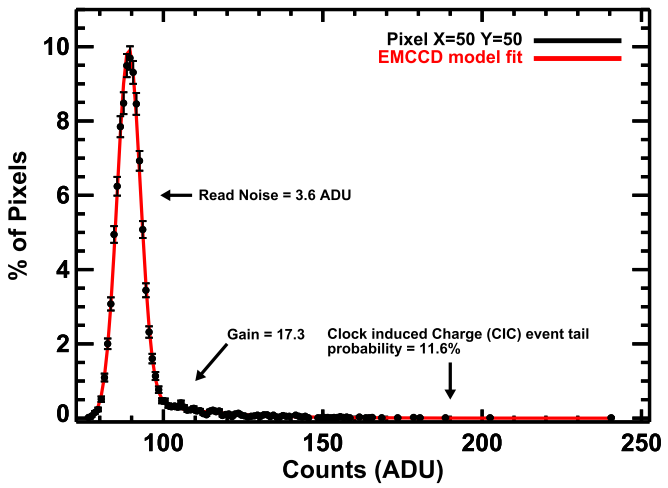

Figure 12. Sample fit to a histogram of a time series of $\approx 10^5$ dark frames for pixel (50, 50), (black circles). The gain, read noise, and clock induced charge rate are derived by fitting an analytic EMCCD model to the data (red line). The analytic EMCCD model (see Section 5.1) is the convolution of the probability that a pixel only has read noise, or has read noise and a clock induced charge event.

comparable to the camera gain setting of 300 for these darks. The read noise, gain, and CIC were similar for the photometric camera. Andor's listed CIC rate of 0.05 events pixel^{-1} frame^{-1} for the cameras is likely underestimated since it does not include CIC events buried within the read noise. A higher CIC rate of 0.08–0.11 events pixel^{-1} frame^{-1} was measured and accounted for CIC within the read noise using the EMCCD model above.

With a derived CIC $p(x, y)$ and gain $G(x, y)$ from fitting dark frames using Equation (11), the dark subtraction algorithm of Harpsøe et al. (2012) was used to subtract the bias count level. First, the mean bias level for each raw frame was computed using pixel 127 to further stabilize the frame to frame bias count variability:

$$b_o(t) = \text{avg}[c(127, y, t) - b(127, y)] \quad (13)$$

where $c(127, y, t)$ are pixel values for the raw frame at pixel $x = 127$. Finally, the bias counts from each raw frame are subtracted as:

$$c_b(x, y, t) = c(x, y, t) - [b(x, y) + b_o(t)] - G(x, y)p(x, y) \quad (14)$$

where $c_b(x, y, t)$ is the bias count subtracted frame.

5.2. Pre-processing Raw Interferograms

Prior to extracting squared visibilities, closure phases, and triple amplitudes from raw interferograms, the following steps are performed:

1. estimate the gain, read noise, and CIC for darks,
2. perform dark subtraction,

3. remove poor quality interferograms, and
4. bin the data spectrally to increase SNR.

First, a series of dark frames taken during the observing sequence (see Section 3.3) is used to estimate the gain, CIC rate, and read noise for the raw interferograms as detailed in Section 5.1 above. Next, dark subtraction is performed using Equation (14) from Section 5.1 above. Raw interferograms for which the fringe tracking SNR is so low that no fringes were identified are removed. This loss of coherence can occur often due to the turbulence of the atmosphere at visible wavelengths. With this step 1%–5% of the raw interferograms that have the lowest fringe SNR (see Section 3.2) are removed. Next, spectral channels with very little light are removed. For stars with spectral types O–F, typically only spectral channels with wavelengths 580–750 nm are used, given that the single-mode fibers enter multimode at <580 nm and spectral channels with wavelengths >750 nm had too little SNR. Next, these spectral channels are binned in the wavelength by a factors of 8, 9, or 10. For a typical 9 spectral channels, this results in an overall read noise of $\sigma_{\mathrm{RN,binned}} = \sqrt{9}\,\sigma_{\mathrm{RN,obs}} \approx 10.5$ ADU, and ≈19 nm per spectral channel. Finally, the raw interferograms are divided by the mean gain as derived above, typically 15–18 ADU/e$^-$.

5.3. Adapting the MIRC Data-processing Pipeline for VISION

Since MIRC and VISION are nearly identical in design, the MIRC data-processing pipeline (Monnier et al. 2004, 2007) was modified to estimate calibrated squared visibilities, closure phases, and triple amplitudes from interferograms pre-processed as detailed in Section 5.2 above. Briefly, the MIRC pipeline measures uncalibrated squared visibilities and triple amplitudes from raw interferograms after a series of Fourier transformations and foreground subtractions. The MIRC pipeline then calibrates the squared visibilities and triple amplitudes using fluxes measured simultaneously with fringes. The last step of the MIRC pipeline is to use calibrators with known sizes to compensate for system visibility drift.

A significant change to the MIRC pipeline for processing VISION interferograms is the use of single 6 ms frames to estimate the uncalibrated squared visibilities. By contrast, MIRC pipeline coherently co-adds several frames of data before estimating uncalibrated squared visibilities. In adapting the MIRC pipeline, the complex bispectrum bias must also be corrected on a frame by frame basis, since VISION data are photon noise limited whereas MIRC data are read-noise limited; the MIRC pipeline only partially implements this correction, since MIRC operates in a regime where photon noise bias in the bispectrum is rarely important.

The uncorrected bispectrum is given as

$$B_{0,ijk} = C_{ij} C_{jk} C_{ki} \tag{15}$$

where $B_{0,ijk}$ is the bispectrum for beams i, j, k, and C_{ij} is the complex discrete Fourier transform for beam pair i, j. The triple product bias was adopted from EMCCD simulations of Basden & Haniff (2004), with an additional read noise term from Gordon & Buscher (2012) that was modified for the EMCCDs:

$$B_{1,ijk} = B_{0,ijk} - 2(|C_{ij}|^2 + |C_{jk}|^2 + |C_{ki}|^2) + 6\,N + 6N_{\mathrm{pix}}\sigma^2_{\mathrm{RN,binned}}. \tag{16}$$

where $|C_{ij}|^2$ is the power spectra, N is the total number of counts in the frame, $N_{\mathrm{pix}} = 128$ is the total number of pixels in the spectral channel, $B_{1,ijk}$ is the bias-corrected bispectrum, and $\sigma_{\mathrm{RN,binned}}$ is the summed read noise in quadrature over the wavelength-binned pixels in Equation (16).

Equation (16) was derived by attempting to recover the correct closure phases extracted from simulated fringes of a binary star with an input orbit, a simulated EMCCD gain register, and added read-noise and Poisson noise. The EMCCD simulations of Basden & Haniff (2004) were replicated, and their Equation (4) was extended by adapting the Gordon & Buscher (2012) treatment of read noise, yielding an extra term of $6N_{\mathrm{pix}}\sigma^2_{\mathrm{RN,binned}}$. Gordon & Buscher (2012) provide equations to correct the bispectrum in the presence of read noise, but their equations only apply for Poission statistics, and the output of the EMCCDs is non-Poissonian due to the stochastiscity of the electron multiplying gain. As detailed in Basden & Haniff (2004), the coefficients of 2 and 6 multiplied by the power spectra $|C_{ij}|^2$ and total counts N in Equation (16) also differ from the traditional Wirnitzer (1985) coefficients of 1 and 2 given that the output from an EMCCD is not Poissonian. The VISION implementation uses the bispectrum bias subtraction in Equation (16) on a frame-by-frame basis as recommended by both Basden & Haniff (2004) and Gordon & Buscher (2012) for extracting unbiased closure phases and triple amplitudes from VISION raw interferograms.

The corrected bispectrum $B_{1,ijk}$ should be zero within error for foreground data, given that these data have no fringes. Therefore, Equation (16) was further tested by comparing the uncorrected bispectrum $B_{0,ijk}$ of a sample set of foregrounds to the theoretical bispectrum bias:

$$B_{0,ijk}\,\text{of Foreground} = -2(|C_{ij}|^2 + |C_{jk}|^2 + |C_{ki}|^2) + 6\,N + 6N_{\mathrm{pix}}\sigma^2_{\mathrm{RN,binned}}. \tag{17}$$

$B_{0,ijk}$ was computed for foreground data from observations of γ Orionis, and it closely matched the right side of Equation (17) above, as shown in Figure 14(a). This further validated that the derived bispectrum bias correction (Equation (16)) for the EMCCDs was correct.

The theoretical prediction for the power spectrum bias was also derived as a modified version of the Gordon & Buscher (2012) power spectrum bias adapted for EMCCDs, in the

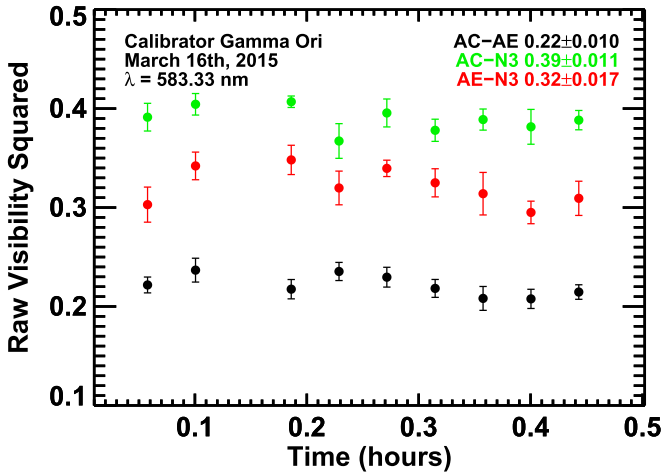

Figure 13. Beam intensity mismatch corrected squared visibilities vs time for observations of calibrator γ Orionis during commissioning on 2015 March 16 with stations AC, AE and N3. The system visibility drift is at max 0.01–0.02 over half an hour for γ Orionis.

presence of read noise:

$$|C_{1,ij}|^2 = |C_{0,ij}|^2 - 2N + N_{\rm pix}\sigma^2_{\rm RN,binned} \quad (18)$$

where $|C_{1,ij}|^2$ is the corrected power spectrum and $|C_{0,ij}|^2$ is the uncorrected power spectrum. Similar to the previous approach, foreground data contains no fringes and therefore no peaks in the power spectrum. Thus, the corrected power spectrum $|C_{1,ij}|^2$ should be zero. The power spectrum bias correction matches the uncorrected power spectrum $|C_{0,ij}|^2$ to within 1% as shown in Figure 14(b).

Table 4
Fringe Searching and Tracking Parameters

EMCCD Exposure Time	6 ms
Effective Coherent Exposure Time	12 ms
Number of Coherent Co-adds	2
Effective In-coherent Exposure Time	360 ms
Number of Incoherent Co-adds	30
Search Step Size	12.5 μm

Note. Fringe searching and tracking parameters detailed in Section 3.1 and Section 3.2. These optimal parameters were determined using on-sky observations in median-seeing conditions.

Table 5
Observations of ζ Orionis

HJD	24557098.122	
UT Date	2015−03−17	
Telescopes Used	AC−AE−N3	
Baseline Length Range	10.77−25.92 m	
Wavelength Range	570–750 nm	
# Closure Phases	35	
$\#V^2$	90	
Median Closure Phase Error	1.°9	
Median V^2 Error	4.5%	
	This Work	Hummel et al. (2013)
Separation (mas)	40.6 ± 1.8	40.1 ± 1.0[a]
Position Angle (deg)	223.°9 ± 1.°0	223.°2 ± 2.°3[a]
ΔMag(570–750 nm)	2.18 ± 0.13	2.2 ± 0.1[a]

Notes. Observations of ζ orionis.
[a] Calculated at HJD = 24557098.122, using orbit of Hummel et al. (2013).

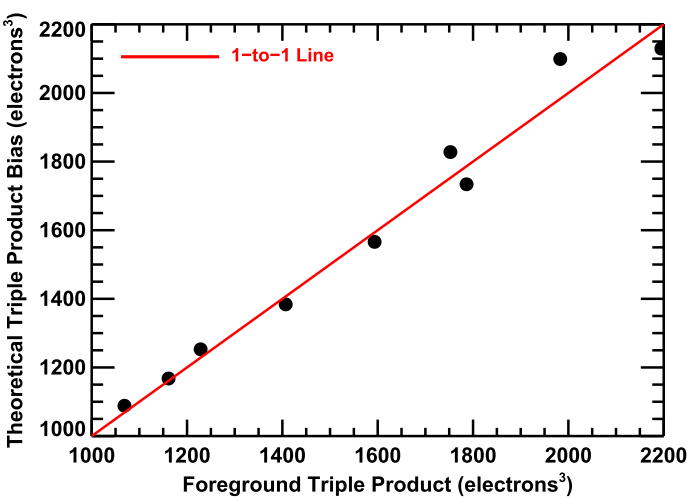

(a) Triple Product Bias

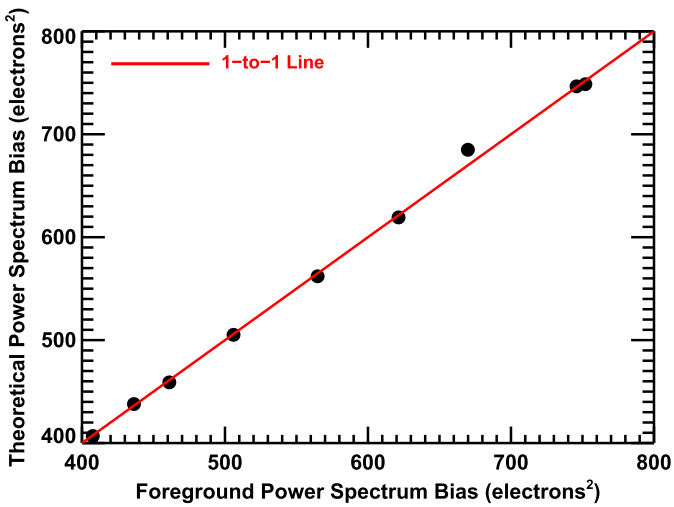

(b) Power Spectrum Bias

Figure 14. The theoretical bispectrum and power spectrum bias match the amplitude of foreground bispectrum and foreground power spectrum for γ Orionis, further verifying that the bias correction procedures in the data-processing pipeline are accurate. The foreground amplitude of the bispectrum and power spectrum were averaged over 15.36 s, using 6 ms exposure times.

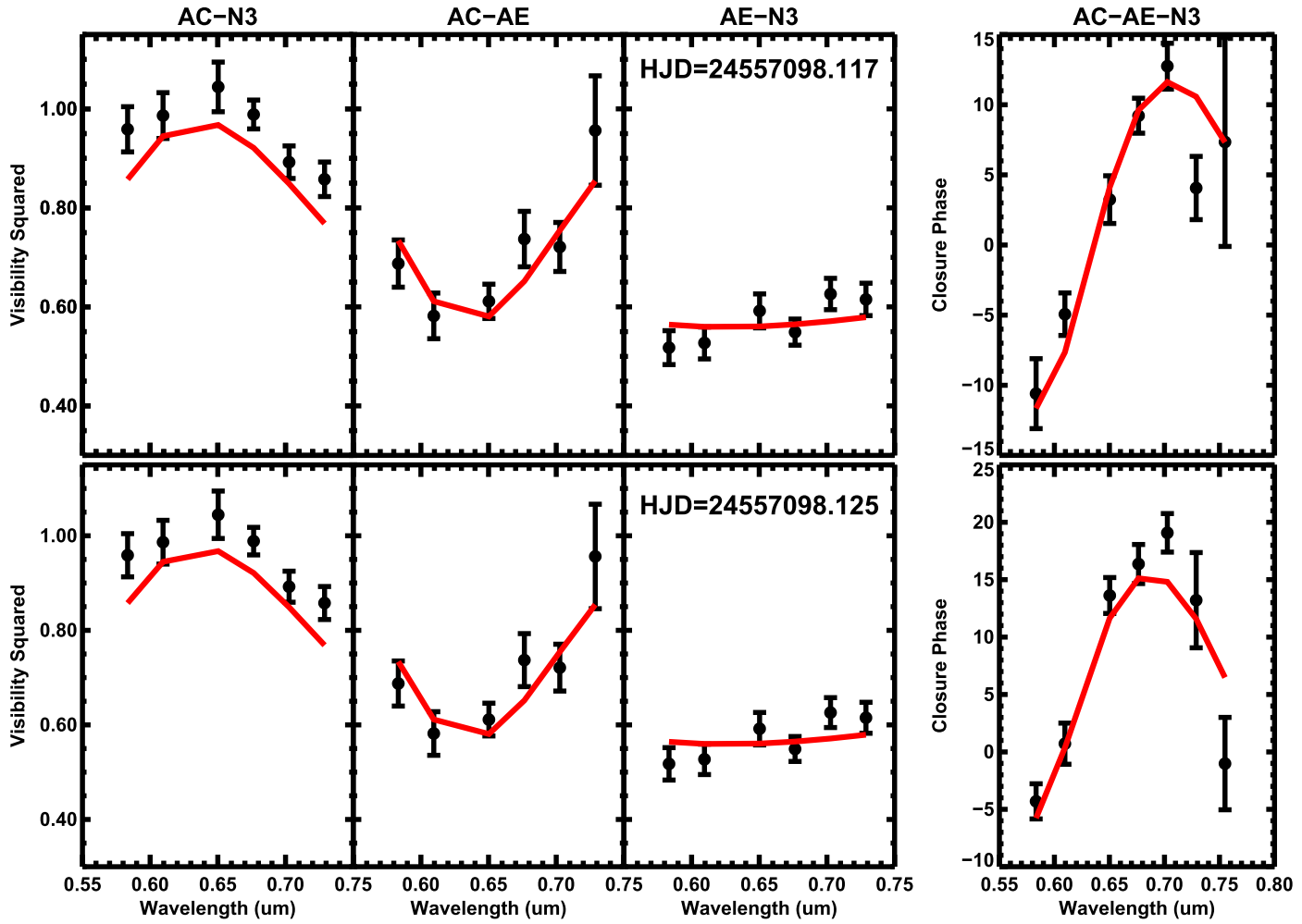

Figure 15. Sample calibrated squared visibilities and closure phase observations of ζ Orionis on UT 03152016 at two different times of the night. The red solid line is the best fit model to the data. the best fit model for this binary star at the epoch the observations yields a separation of 40.6 ± 1.8 mas, a position angle of 223.°9 ± 1.°0 for observations from 580 to 750 nm, in good agreement with the predicted separation of 40.1 ± 1.0 mas and position angle 223.2 ± 2.3 mas from Hummel et al. (2013). The observed flux ratio of 2.18 ± 0.13 mag is also in good agreement with the flux ratio 2.2 ± 0.1 mag from Hummel et al. (2013). The AC-N3 visibilities have a small bias likely due possibly to imperfect photometric calibration.

6. The Orbit and Flux Ratio of ζ Orionis A

To both provide a first on-sky science result and to verify the VISION data-processing pipeline from Section 5.2 and Section 5.3, VISION was used to obtain new resolved observations of the massive binary star ζ Orionis A. The orbit and flux ratio of ζ Orionis A have previously been measured by Hummel et al. (2013), therefore the new observations serve as an established test of the VISION system and provide an additional epoch of constraint on the orbit of this benchmark astrometric binary.

ζ Orionis A was observed on 2015 March 16th, with stations AC, AE and N3, with baselines between 10.77 and 25.92 m using the observation sequence in Table 2. Fringe searching and tracking were performed as described in Section 3.1 and Section 3.2. The calibrator star γ Orionis ($\theta_{UD} = 0.701 \pm 0.005$; Challouf et al. 2014) was observed immediately after, using the same observing sequence to compensate for any visibility drift. The wavelength solutions for the cameras from Section 2.1 was used.

Sample squared visibilities versus time for γ Orionis are shown in Figure 13. The squared visibility drift for VISION as measured using γ Orionis is 0.01–0.02 over 30 minutes. Dark subtraction was performed on all the raw frames of ζ Orionis and the calibrator γ Orionis as described in Section 5.1. The data were pre-processed as described in Section 5.2 and calibrated squared visibilities and bias-corrected closure phases were extracted as described in Section 5.3.

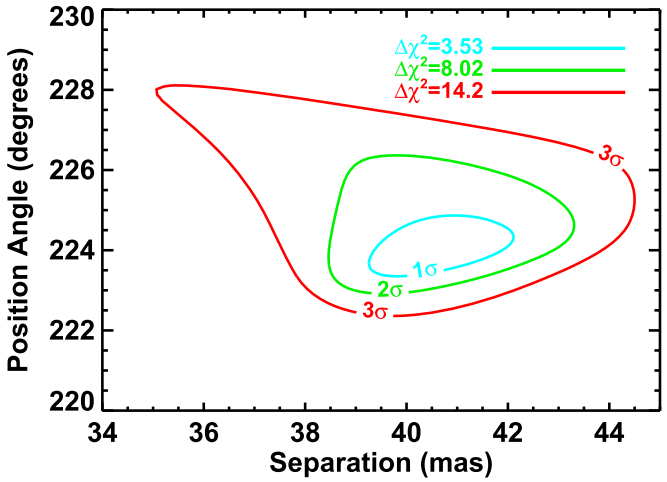

Figure 16. Confidence intervals for 1σ (blue line), 2σ (green line) and 3σ (red line) errors on the separation and position angle corresponding to $\Delta\chi^2 = \chi^2 - \chi^2_{\rm min}$ of 3.53, 8.02 and 14.03 respectively for 3 parameters of interest (Press et al. 2002). The minimum $\chi^2_{\rm min}$ corresponds to the best fit model (red solid line) in Figure 15.

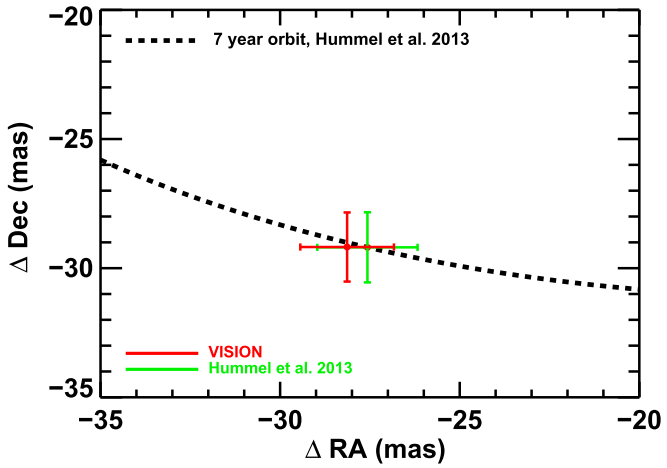

Figure 17. The observed position angle and separation for the binary ζ Orionis A (red) match the known orbit Hummel et al. (2013) (black line). The errors on the predicted ΔR.A. and ΔDecl. (green) was calculated from the error on the orbital elements from Hummel et al. (2013).

From the orbit of Hummel et al. (2013), ζ Orionis A is predicted to have a separation of 40.1 ± 1.0 mas and a position angle of $223\overset{\circ}{.}2 \pm 2\overset{\circ}{.}3$ at the epoch of the observations, with a flux ratio of 2.2 ± 0.1 mag. The 1σ errors on the predicted separation and position angle were calculated from distributions of separation and position angle from 10^7 uniformly randomly selected orbits from the reported 1σ errors of the orbital elements from Hummel et al. (2013) and then projected on sky.

The new observations of ζ Orionis A with VISION yield a best-fit separation of 40.6 ± 1.8 mas, a position angle of $223\overset{\circ}{.}9 \pm 1\overset{\circ}{.}0$, and flux ratio of 2.18 ± 0.13 mag at 580–750 nm and are listed in Table 5. A sample of the extracted squared visibilities and closure phases along with the best fit model are shown in Figure 15. The median error on the closure phase is $1\overset{\circ}{.}9$ and on V^2 is 4.5%. The error increases toward redder wavelengths due to decreased SNR, which is in part due to a decrease in quantum efficiency of 83% to 73% from 600 to 750 nm. The formal 1σ errors were plotted on the fitted orbit and flux ratio using 1σ confidence intervals with $\Delta\chi^2 = \chi^2 - \chi^2_{\rm min} = 3.53$, which corresponds to 1σ for 3 parameters of interested (Press et al. 2002). The 1σ, 2σ, and 3σ confidence intervals for the fitted orbit to ζ Orionis are shown in Figure 16. Finally, as shown in Figure 17, there is excellent agreement between the observed separation and position angle for ζ Orionis A as observed by VISION versus that predicted by the previously published orbit (Hummel et al. 2013).

7. Conclusions and Future Work

This paper introduces the VISION beam combiner for NPOI: a six-telescope image plane combiner featuring optical fibers, electron multiplying CCDs, and real-time photometric monitoring of each beam for visibility calibration. The VISION cameras, the fringe crosstalk, and the system visibility have been characterized, and a version of the MIRC data-processing pipeline has been adapted and verified for VISION with an observation of the benchmark astrometric binary star ζ Orionis A.

Future work on the instrument includes installation of new Nüvü cameras with 10 times less clock-induced charge noise. Recently, the 750 mm fringe-forming lens was replaced with a 500 mm lens to fully sample the Gaussian profile on the fringing camera, with early indications showing a gain of 30% flux, as well as a significant reduction in fringe crosstalk. Finally, the control system code will be updated from a text user interface to a graphical user interface.

With the capabilities demonstrated here, we anticipate now being able to use VISION to make the first 5- or 6-telescope reconstructed images at visible wavelengths of the main sequence stars Altair and Vega, as well observations of triple star systems and the TiO lines on the surfaces of spotted red supergiant stars.

E.V.G. would like to acknowledge the gracious support of his Lowell Pre-doctoral Fellowship by the BF foundation. E.V.G. would also like to acknowledge the support received from the Fisk-Vanderbilt Masters-PhD program. This work was supported by NSF-AST 0958267 "MRI-R^2 Consortium: Development of VISION: The Next Generation Science Camera for the Navy Prototype Optical Interferometer." We gratefully acknowledge the VISION instrument PI team at

TSU, led by Matthew Muterspaugh. This research has made use of the SIMBAD database, operated at CDS, Strasbourg, France. The work done with the NPOI was performed through a collaboration between the Naval Research Lab and the US Naval Observatory, in association with Lowell Observatory, and was funded by the Office of Naval Research and the Oceanographer of the Navy.

References

Armstrong, J. T., Jorgensen, A. M., Neilson, H. R., et al. 2012, Proc. SPIE, 8445, 84453K
Armstrong, J. T., Mozurkewich, D., Pauls, T. A., & Hajian, A. R. 1998a, Proc. SPIE, 3350, 461
Armstrong, J. T., Mozurkewich, D., Rickard, L. J., et al. 1998b, ApJ, 496, 550
Armstrong, J. T., Nordgren, T. E., Germain, M. E., et al. 2001, AJ, 121, 476
Baines, E. K., Armstrong, J. T., Schmitt, H. R., et al. 2014, ApJ, 781, 90
Baines, E. K., Armstrong, J. T., & van Belle, G. T. 2013, ApJL, 771, L17
Baron, F., Monnier, J. D., Kiss, L. L., et al. 2014, ApJ, 785, 46
Basden, A. G., & Haniff, C. A. 2004, MNRAS, 347, 1187
Bazot, M., Ireland, M. J., Huber, D., et al. 2011, A&A, 526, L4
Berger, J.-P., Haguenauer, P., Kern, P. Y., et al. 2003, Proc. SPIE, 4838, 1099
Born, M., & Wolf, E. 1999, Principles of Optics: Electromagnetic Theory of Propagation, Interference and Diffraction of Light (Cambridge: Cambridge Univ. Press)
Challouf, M., Nardetto, N., Mourard, D., et al. 2014, A&A, 570, A104
Che, X., Monnier, J. D., Zhao, M., et al. 2011, ApJ, 732, 68
Chiavassa, A., Bigot, L., Kervella, P., et al. 2012, A&A, 540, A5
Chiavassa, A., Haubois, X., Young, J. S., et al. 2010, A&A, 515, A12
Chiavassa, A., Pasquato, E., Jorissen, A., et al. 2011, A&A, 528, A120
Chiavassa, A., Plez, B., Josselin, E., & Freytag, B. 2009, A&A, 506, 1351
Coudé du Foresto, V., Ridgway, S., & Mariotti, J.-M. 1997, A&AS, 121, 379
Davis, J., Tango, W. J., Booth, A. J., et al. 1999a, MNRAS, 303, 773
Davis, J., Tango, W. J., Booth, A. J., Thorvaldson, E. D., & Giovannis, J. 1999b, MNRAS, 303, 783
Domiciano de Souza, A., Hadjara, M., Vakili, F., et al. 2012, A&A, 545, A130
Domiciano de Souza, A., Kervella, P., Jankov, S., et al. 2003, A&A, 407, L47
Ducati, J. R. 2002, yCat, 2237, 0
Espinosa Lara, F., & Rieutord, M. 2011, A&A, 533, A43
Espinosa Lara, F., & Rieutord, M. 2013, A&A, 552, A35
Freytag, B., & Höfner, S. 2008, A&A, 483, 571
Freytag, B., Steffen, M., & Dorch, B. 2002, AN, 323, 213
Frigo, M., & Johnson, S. G. 2005, Proc. IEEE, 93, 216
Ghasempour, A., Muterspaugh, M. W., Hutter, D. J., et al. 2012, Proc. SPIE, 8445, 84450M
Gordon, J. A., & Buscher, D. F. 2012, A&A, 541, A46
Harpsøe, K. B. W., Jørgensen, U. G., Andersen, M. I., & Grundahl, F. 2012, A&A, 542, A23
Haubois, X., Perrin, G., Lacour, S., et al. 2009, A&A, 508, 923
Huber, D., Ireland, M. J., Bedding, T. R., et al. 2012a, ApJ, 760, 32
Huber, D., Ireland, M. J., Bedding, T. R., et al. 2012b, MNRAS, 423, L16
Hummel, C. A., Benson, J. A., Hutter, D. J., et al. 2003, AJ, 125, 2630
Hummel, C. A., Carquillat, J.-M., Ginestet, N., et al. 2001, AJ, 121, 1623
Hummel, C. A., Mozurkewich, D., Armstrong, J. T., et al. 1998, AJ, 116, 2536
Hummel, C. A., Rivinius, T., Nieva, M.-F., et al. 2013, A&A, 554, A52
Ireland, M. J., Mérand, A., ten Brummelaar, T. A., et al. 2008, Proc. SPIE, 7013, 24
Jamialahmadi, N., Berio, P., Meilland, A., et al. 2015, A&A, 579, A81
Jorgensen, A. M., Mozurkewich, D., & Hutter, D. 2014, in ASP Conf. Ser. 487, Resolving The Future Of Astronomy With Long-Baseline Interferometry, ed. M. J. Creech-Eakman, J. A. Guzik, & R. E. Stencel (San Francisco, CA: ASP), 303
Jorgensen, A. M., Mozurkewich, D., Schmitt, H., et al. 2006, Proc. SPIE, 6268, 62681H
Kloppenborg, B., Stencel, R., Monnier, J. D., et al. 2015, ApJS, 220, 14
Kok, Y., Ireland, M. J., Tuthill, P. G., et al. 2012, Proc. SPIE, 8445, 844521
Landavazo, M. I., Jorgensen, A. M., Sun, B., et al. 2014, Proc. SPIE, 9146, 914621
Maestro, V., Che, X., Huber, D., et al. 2013, MNRAS, 434, 1321
Maestro, V., Kok, Y., Huber, D., et al. 2012, Proc. SPIE, 8445, 84450G
Markwardt, C. B. 2009, in ASP Conf. Ser. 411, Astronomical Data Analysis Software and Systems XVIII, ed. D. A. Bohlender, D. Durand, & P. Dowler (San Francisco, CA: ASP), 251
Monnier, J. D., Berger, J.-P., Millan-Gabet, R., & ten Brummelaar, T. A. 2004, Proc. SPIE, 5491, 1370
Monnier, J. D., Che, X., Zhao, M., et al. 2012, ApJL, 761, L3
Monnier, J. D., Pedretti, E., Thureau, N., et al. 2006, Proc. SPIE, 6268, 62681P
Monnier, J. D., Zhao, M., Pedretti, E., et al. 2007, Sci, 317, 342
Mourard, D., Bério, P., Perraut, K., et al. 2011, A&A, 531, A110
Mourard, D., Challouf, M., Ligi, R., et al. 2012, Proc. SPIE, 8445, 84450K
Mourard, D., Clausse, J. M., Marcotto, A., et al. 2009, A&A, 508, 1073
Mourard, D., Perraut, K., Bonneau, D., et al. 2008, Proc. SPIE, 7013, 23
Mozurkewich, D. 1994, Proc. SPIE, 2200, 76
Muterspaugh, M. W., Fekel, F. C., Lane, B. F., et al. 2010, AJ, 140, 1646
Muterspaugh, M. W., Lane, B. F., Fekel, F. C., et al. 2008, AJ, 135, 766
Muterspaugh, M. W., Lane, B. F., Konacki, M., et al. 2005, AJ, 130, 2866
Muterspaugh, M. W., Lane, B. F., Konacki, M., et al. 2006a, A&A, 636, 1020
Muterspaugh, M. W., Lane, B. F., Konacki, M., et al. 2006b, ApJ, 652, 1469
Muterspaugh, M. W., Lane, B. F., Kulkarni, S. R., et al. 2006c, ApJ, 446, 723
North, J. R., Davis, J., Robertson, J. G., et al. 2009, MNRAS, 393, 245
North, J. R., Tuthill, P. G., Tango, W. J., & Davis, J. 2007, MNRAS, 377, 415
Ohishi, N., Nordgren, T. E., & Hutter, D. J. 2004, ApJ, 612, 463
Patience, J., Zavala, R. T., Prato, L., et al. 2008, ApJL, 674, L97
Peterson, D. M., Hummel, C. A., Pauls, T. A., et al. 2006, Natur, 440, 896
Petrov, R. G., Malbet, F., Weigelt, G., et al. 2007, A&A, 464, 1
Press, W. H., Teukolsky, S. A., Vetterling, W. T., & Flannery, B. P. 2002, Numerical Recipes in C++: the Art of Scientific Computing (Cambridge: Cambridge Univ. Press)
Ragland, S., Traub, W. A., Berger, J.-P., et al. 2004, Proc. SPIE, 5491, 1390
Roettenbacher, R. M., Monnier, J. D., Fekel, F. C., et al. 2015a, ApJ, 807, 23
Roettenbacher, R. M., Monnier, J. D., Henry, G. W., et al. 2015b, ApJ, 809, 159
Rousselet-Perraut, K., Haguenauer, P., Petmezakis, P., et al. 2000, Proc. SPIE, 4006, 1042
Rousselet-Perraut, K., Stadler, E., Feautrier, P., et al. 1999, in ASP Conf. Ser. 194, Working on the Fringe: Optical and IR Interferometry from Ground and Space, ed. S. Unwin, & R. Stachnik (San Francisco, CA: ASP), 344
Schmitt, H. R., Pauls, T. A., Tycner, C., et al. 2009, ApJ, 691, 984
Shaklan, S., & Roddier, F. 1988, ApOpt, 27, 2334
Shaklan, S. B., Colavita, M. M., & Shao, M. 1992, in European Southern Observatory Conf. and Workshop Proc. 39, Visibility Calibration using Single Mode Fibers in a Long-baseline Interferometer, ed. J. M. Beckers, & F. Merkle, 1271
Sun, B., Jorgensen, A. M., Landavazo, M., et al. 2014, Proc. SPIE, 9146, 20
Tango, W. J., Davis, J., Jacob, A. P., et al. 2009, MNRAS, 396, 842
ten Brummelaar, T. A., McAlister, H. A., Ridgway, S. T., et al. 2005, ApJ, 628, 453
Traub, W. A., Berger, J.-P., Brewer, M. K., et al. 2004, Proc. SPIE, 5491, 482
van Belle, G. T. 2012, A&AR, 20, 51
Wang, X., Hummel, C. A., Ren, S., & Fu, Y. 2015, AJ, 149, 110
Wenger, M., Ochsenbein, F., Egret, D., et al. 2000, A&AS, 143, 9
White, T. R., Huber, D., Maestro, V., et al. 2013, MNRAS, 433, 1262
Wirnitzer, B. 1985, JOSAA, 2, 14
Wittkowski, M., Hummel, C. A., Aufdenberg, J. P., & Roccatagliata, V. 2006, A&A, 460, 843
Zavala, R. T., Hummel, C. A., Boboltz, D. A., et al. 2010, ApJL, 715, L44
Zhang, X., Armstrong, J. T., Clark, J. A., III, et al. 2006, Proc. SPIE, 6268, 62683V
Zhao, M., Gies, D., Monnier, J. D., et al. 2008, ApJL, 684, L95